University of Louisville

ThinkIR: The University of Louisville's Institutional Repository

Electronic Theses and Dissertations

8-2011

Numerical investigation of the aerodynamic characteristics of a flat plate in an oscillating freestream.

Russell Prater
University of Louisville

Follow this and additional works at: https://ir.library.louisville.edu/etd

NUMERICAL INVESTIGATION OF THE AERODYNAMIC CHARACTERISTICS OF A
FLAT PLATE IN AN OSCILLATING FREESTREAM

By

Russell Prater
B.S. Eng, University of Louisville, 2011

A Thesis
Submitted to the Faculty of
University of Louisville
J.B. Speed School of Engineering
On Partial Fulfillment of Requirements
For the Professional Degree

Master of Engineering

Department of Mechanical Engineering

August 2011

NUMERICAL INVESTIGATION OF THE AERODYNAMIC CHARACTERISTICS OF A
FLAT PLATE IN AN OSCILLATING FREESTREAM

Submitted by: _____
Russell Prater

A Thesis Approved By:

_____
(Date)

by the Following Reading and Examination Committee:

_____
Dr. Yongsheng Lian, Thesis Director

_____
Dr. Roger Bradshaw

_____
Dr. Tim Dowling

_____
Dr. Sam Park

ACKNOWLEDGMENTS

ABSTRACT

Micro air vehicles (MAVs) are type of unmanned aircraft with a maximum length of 150 mm (6 in.) and flight speed of less than 10 m/s. Because their flight speed is comparable to the environmental wind speed coupled with their small size and low inertia, MAVs are sensitive to variations in the wind speed leading to a need to plan for flight control mechanisms to counteract these variations. In order to develop efficient control schemes it is necessary to understand the aerodynamic responses elicited in the vehicle from wind speed variations.

In this thesis, the flight characteristics of a flat plate in low Reynolds number flow with gusting conditions are examined both numerically and using a theoretical approach. The aerodynamic forces are numerically solved using an incompressible Navier-Stokes solver on an overlapping grid using the pressure-Poisson method. The impact of reduced frequency of the oscillations in the flow on the phase between oscillating freestream and lift, time averaged lift and lift oscillation amplitude are discussed in detail. Comparisons are made with experimental measurements and theoretical predictions to examine the validity of using a theoretical prediction for the force response to a wind gust. This thesis shows that theoretical results match the numerical results when both the reduced frequency and angle of attack (AoA) is low. At high angles of attack or high reduced frequencies, flow separation and periodic vortex shedding occurs and the theoretical model shows significant difference from the numerical simulations. The reason for the discrepancies is that the theoretical model is based on potential flow which doesn't allow for the possibility of flow separation, which is shown to occur at these higher angles of attack and reduced frequencies.

The numerical simulations show that the time averaged lift increases with reduced frequency. At high reduced frequencies the lift response, in the cases tested, is up to 80° out of phase with the freestream velocity. The peak-to-peak lift amplitude varies with the reduced frequency and it peaks at a value which depends on the angle of attack while the phase increases with the reduced frequency. Also discussed is the possibility that the numerical simulations are experiencing an early onset of a Hopf bifurcation brought on by the oscillating freestream. It is possible that the early onset of the bifurcation is magnifying the aerodynamic responses observed in the flat plate simulations.

NOMENCLATURE

a_u = Amplitude of freestream oscillation, m/s

a_L = Amplitude of lift force, N, defined as the difference between the maximum and time averaged lift

b = A quarter of the chord length

B = Boundary condition

c = Chord length

C_L = Coefficient of lift

D = Domain

f = Frequency of freestream oscillation, Hz

g = Gravitational constant

k = Reduced frequency $= \pi f c / u$

L = Lift

L_0 = Lift from non-oscillating freestream velocity

m = Volume flow rate per unit length

p = Pressure

Re = Reynolds Number

t = Time, seconds

T = Gust oscillation period

u = Freestream velocity

u_0 = Mean freestream velocity

U = Circulation magnitude

w	=	Local velocity
α	=	Angle of attack (AoA)
ρ	=	Density
ϕ	=	Velocity potential
τ	=	Shear stress
μ	=	Dynamic viscosity
ν	=	Kinematic viscosity
Γ	=	Circulation

TABLE OF CONTENTS

LIST OF TABLES

Table I

LIST OF FIGRURES

I. INTRODUCTION

A. Background

There is a growing interest in developing Micro Air Vehicles (MAVs) for both civil and military applications in urban environments with numerous applications including search and rescue or reconnaissance. Urban environments are typically characterized by their turbulent nature due to being significantly impacted by the influence of the atmospheric boundary layer, and by the surface frictional effect (Watkins et al. 2006). Long term studies of the an Australian city at a height of 10 meters suggests the average wind speed is approximately 4 m/s (Bowen et al., 1983). Environments with terrain roughness between 4 (areas such as villages, suburban terrain or permanent forests) and 7 (an area with at least 15% of the area covered by objects with an average height exceeding 15m) have a general turbulence range between 15% and 35% of the mean flow speed and spectra ranges between 0.25 and 2.5 Hz (Watkins et al., 2003) with the peaks in turbulence occurring around a gust frequency of 1 Hz. The turbulence that characterizes the environments has become a major constraint in MAV operation because MAVs have much lower inertia than traditional aircraft (Spedding et al., 1998). Variations in the freestream velocity can greatly impact the flight stability and lead to variation in position which becomes important when either steady flight or precise maneuvering is required of the MAV.

Previous studies (Lissaman, 2005, Patel, 2006, Langelaan and Bramesfeld, 2008, and Lissaman and Patel, 2007) examined the effects of gusting on aerial vehicles and concluded that

during the gusting occurrences energy could be extracted. The energy extraction can potentially improve vehicle flight duration and reduce the energy requirements.

Previous studies on the effects of gusting on a semi-circular wing at chord based Reynolds numbers between 42,000 and 70,600 (Williams et al., 2009a,b) looked at the phase between the lift and the oscillating freestream and found that the phase was dependent on both the angle of attack (AoA) and the dimensionless frequency (k) of the gusting flow field. Based on these findings, they developed a feed forward controller to suppress the lift oscillations. They showed that using a system of pulsed-blowing jets to modify the flow around the leading edge and wing tips could increase the lift coefficient and delay stall at higher angles of attack when compared to the same model without flow control. Williams et al. provided experimental data of a flat plate at the same Reynolds numbers that the numerical data was corroborated against.

In this thesis, a numerical study of wind gust on the aerodynamic performance of a two-dimensional flat plate in low Reynolds number flows is performed. The goal is to understand the influence of wind gust on the aerodynamic performance of MAVs and to verify whether theoretical prediction (Theodorsen, 1935, Greenberg, 1947) can be applied to predict the flight aerodynamics under a gusting wind flow. The dependence of phase lag, peak-to-peak lift amplitude on the angle of attack, wind gust frequency, and oscillation amplitude will be investigated.

B.   Literature Review – Theoretical Derivation

This section details the development of the theoretical equation used to evaluate the

effect of an oscillating freestream on the lift of a flat plate. The theory is developed from

potential flow theory by superpositioning oscillating flow and circulation about a flat plate. The

derivation is adapted from NACA report 496 (Theodoreson 1935) and NACA report 1326

(Greenberg 1947). Because the theory is based on potential flow it is assumed that the flow is

inviscid, irrotational and incompressible.

1.   Transformation From a Physical to a Computational Domain

The theory is developed by first defining the geometry of a flat plate as well as its modes

of movement as in Figure 1 where α is the angle of attack (held constant) and u is a fluid

velocity far away from the flat plate that is time dependent.   The generalized case is developed

from a flat plate with an angle of attack zero such that it lies on the u-axis (note: the horizontal

axis is denoted as u to denote the x-axis used prior to a conformal mapping transformation) as in

Figure 2. Parameter b is a constant equal to ¼ of the chord length.
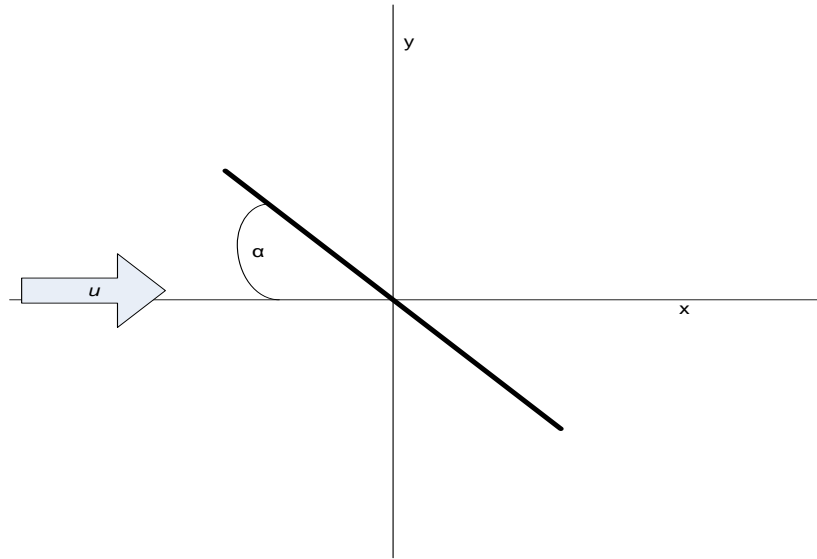
Figure 1 – A Flat Plate Forms an Angle with the Incoming Flow.
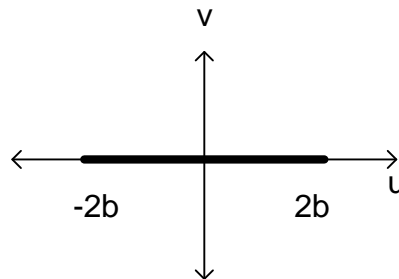
Figure 2 – A Flat Plate with an AoA of Zero.

A conformal mapping transformation is used to transform the flat plate arrangement into a plane where the case is easier mathematically to solve. The two planes used are the x-y plane and the v-u plane. An example of this conversion is presented in Figure 3.
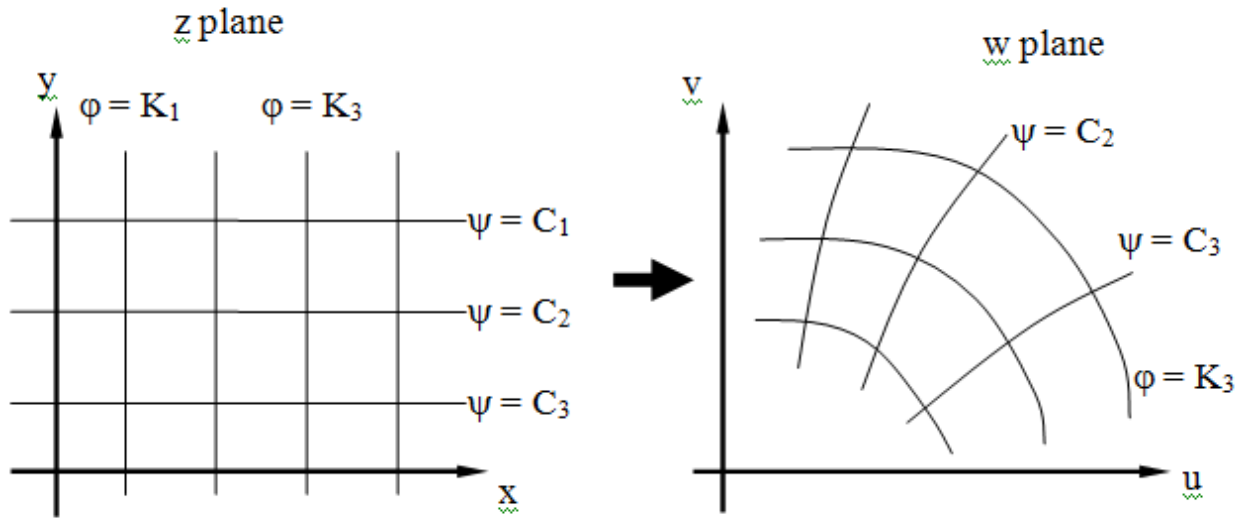
Figure 3 – Stream Function and Velocity Potential in the z Plane (left) and the w Plane (right)

The w plane is defined as

$$w = u + iv \qquad (1)$$

and the z plane is defined as

$$z = x + iy \qquad (2)$$

For the transformation between the two planes the Joukowski transformation is used wherein

$$w = z + \frac{b^2}{z} \qquad (3)$$

The flat plate shown above, is defined as

$$w = 2b\cos(\theta) \quad 0 < \theta \le 2\pi \qquad (4)$$

and describes the line segment $-2b \le u \le 2b$. Following use of the Joukowski transformation the line segment is transformed into a circle in the z plane defined by equation 5 and shown graphically in Figure 4.

5

$$z = \mathrm{b}e^{i\theta} \tag{5}$$
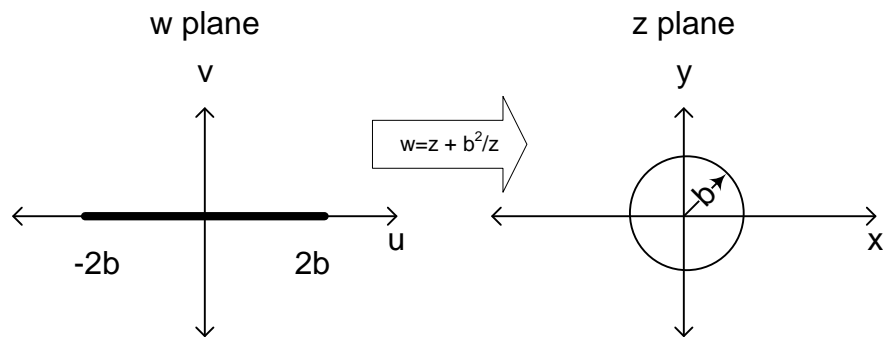
Figure 4 – Graphical Conversion between z and w Plane

2. Velocity Potential Due to a Uniform Oscillating Flow

The velocity potentials arising from uniform flow around the flat plate are developed for a general case by assuming the boundary of the transformed flat plate can be represented as a series of sources and sinks (see Figure 5) with the sources and sinks being located at some point (x_1, y_1) on the boundary.
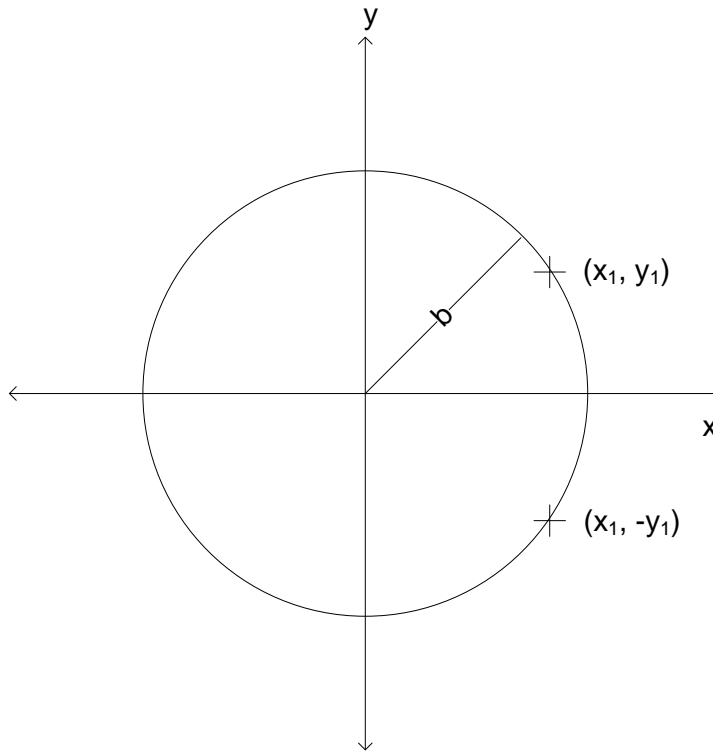
Figure 5 – Circle Arrangement in x-y Plane Centered at the Origin with Radius b

To develop the potential flow around the circle in the z plane, the potential of a source is described by considering fluid flowing outward radially from a source

$$u_r = \frac{m}{2\pi r} \tag{6}$$

where m is a volume flow rate per unit length. Graphically this is shown as in Figure 6.
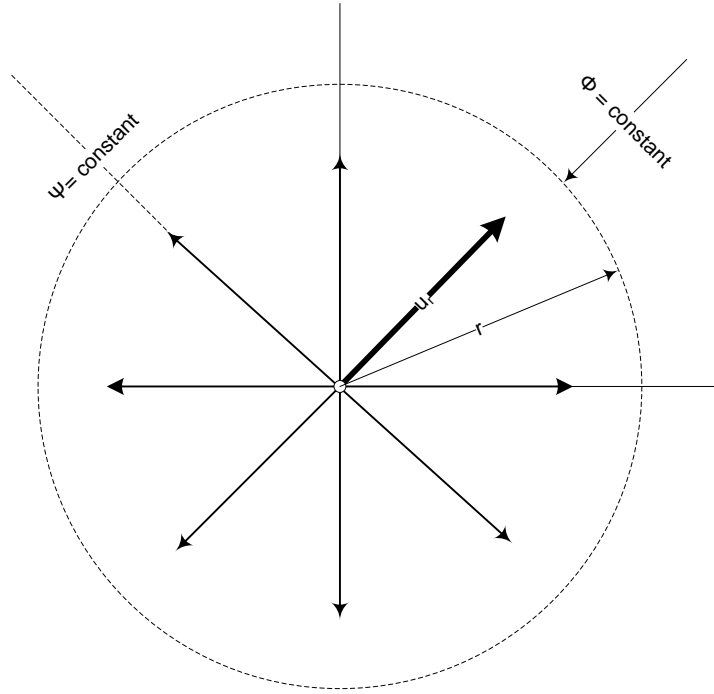
Figure 6 – Streamline Pattern for a Source

Because the flow is purely radial (i.e. $v_\theta = 0$), the corresponding velocity potential, ϕ, can be obtained by integration of

$$\frac{\partial \phi}{\partial r} = \frac{m}{2\pi r} \qquad \frac{1}{r}\frac{\partial \phi}{\partial \theta} = 0 \tag{7}$$

The velocity potential in the Cartesian coordinates is given as

$$\phi = \frac{m}{4\pi}\ln(x^2 + y^2) \tag{8}$$

8

Hence the velocity potential at a point (x, y) by a source of strength m located at any point (x_1, y_1) is given by

$$\phi(x, y) = \frac{m}{4\pi} \ln[(x - x_1)^2 + (y - y_1)^2] \qquad (9)$$

Equation 9 describes a positive double source term along the upper half of the circle in Figure 5. Adding to this a negative double source on the lower half of the circle in Figure 5 [or a negative source at point (x_1, -y_1)] yields

$$\phi = \frac{m}{2\pi} \ln \frac{(x - x_1)^2 + (y - y_1)^2}{(x - x_1)^2 + (y + y_1)^2} \qquad (10)$$

A double source is used because, referring back to Figure 6, the volume flow rate term, m, is equally distributed outward along the entire 2π radians. If a source is only applied above a flat plate (as in Figure 7), then the volume flow rate term is equally distributed along only π radians rather than 2π radians.
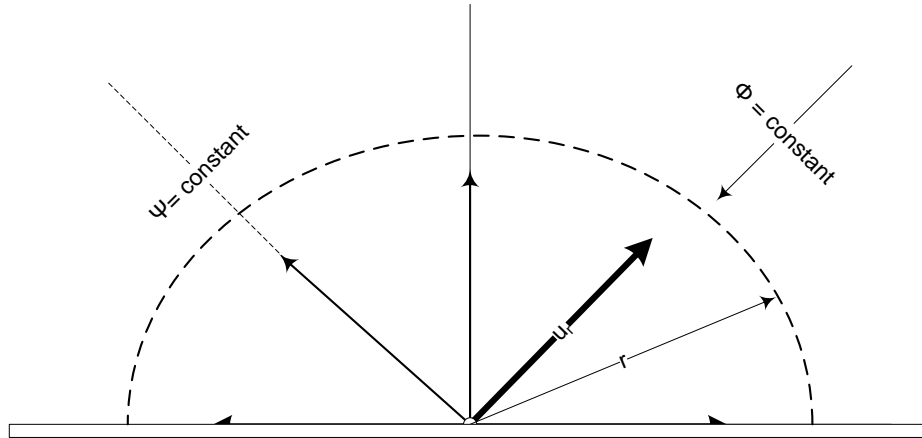
Figure 7 - Source on Surface of a Flat Plate

Since the geometry being worked with is circular, y_1 can be written in terms of x_1 using

$$y_1 = \pm\sqrt{\mathrm{b}^2 - x_1^2} \qquad (11)$$

The potential can be written and evaluated as a function purely in x_1 terms, and assuming m is a constant, the potential can be obtained from the summation of an infinite number of sources along the circle. Because the interest is the potential along the surface of the airfoil a further substitution is made to write y in terms of x so the equation for the potential over the top half of surface is only in terms of x:

$$y = \sqrt{\mathrm{b}^2 - x^2} \qquad (12)$$

Evaluation of equation 10 with this substitution reduces to

$$\phi_{top} = m\sqrt{\mathrm{b}^2 - x^2} \qquad (13)$$

For the potential over the bottom the substitution

$$y = -\sqrt{\mathrm{b}^2 - x^2} \qquad (14)$$

is instead made and the potential is

$$\phi_{bottom} = -m\sqrt{\mathrm{b}^2 - x^2} \qquad (15)$$

or

$$\phi_{top} = -\phi_{bottom} \qquad (16)$$

Since a stationary flat plate is being considered, the only thing that influences the potential is the flat plate orientation relative to a zero degree angle with a clockwise rotation (considered a positive angle of attack) and a purely horizontal velocity, u, in the positive direction. The strength of the source resulting from this is

$$m_\alpha = u\alpha\mathrm{b} \qquad (17)$$

10

Substitution into equation 15 gives the potential along the surface of the flat plate arising from the flat plate orientation with respect to a flow velocity:

$$\phi_\alpha = u\alpha b\sqrt{b^2 - x^2} \tag{18}$$

Having derived the velocity potentials along the flat plate, surface local pressures can be calculated, and integrated to yield the forces acting on the flat plate.

The assumptions of constant fluid density, ρ, and irrotational flow permits the use of the unsteady form of the Bernoulli equation:

$$\frac{\partial \phi}{\partial t} + \frac{1}{2}w^2 + \frac{p}{\rho} + gz = 0 \tag{19}$$

where w is the local velocity magnitude. Neglecting gravitational effects, equation 16 can be rearranged to solve for the pressure.

$$p = -\rho(\frac{w^2}{2} + \frac{\partial \phi}{\partial t}) \tag{20}$$

Making the substitution of

$$w = u + \frac{\partial \phi}{\partial x} \tag{21}$$

to put the local velocity in terms of the flow velocity and the change in potential in terms of the change of x (Theodorsen, 1935) and making use of equation 16, the difference between the pressure on the top and the bottom of the flat plate is

$$\triangle p = -2\rho(u\frac{\partial \phi}{\partial x} + \frac{\partial \phi}{\partial t}) \tag{22}$$

To evaluate this integral, the derivative of equation 18 is taken with respect to x, noting that α is constant along the airfoil:

$$\frac{\partial \phi_\alpha}{\partial x} = \frac{-x u \alpha \mathrm{b}}{\sqrt{\mathrm{b}^2 - x^2}} \tag{23}$$

Equation 18 is then differentiated with respect to time, this time allowing *u* to vary with time.

$$\frac{\partial \phi_\alpha}{\partial t} = -\dot{u}\alpha \mathrm{b}\sqrt{\mathrm{b}^2 - x^2} \tag{24}$$

Substitution of equations 23 and 24 into equation 22 followed by integrating over the

transformed flat plate length gives the force as

$$L = \int_{-\mathrm{b}}^{\mathrm{b}} \triangle p = \frac{-\pi}{2}\dot{u}\alpha \mathrm{b}^2 \tag{25}$$

12

3. Velocity Potential Due to Circulation

It is known that airfoils in flow shed vortices and the circulatory effects of these vortices influence the circulation around the airfoil which in turn affects the velocity potential and hence the lift. To capture the impact of this effect, the wake is visualized as a vortex with irrotational motion (Figure 8) such that

$$\phi = K\theta$$
$$\psi = - K \ln r$$

(26)

and *K* is a constant related to the vortex strength.
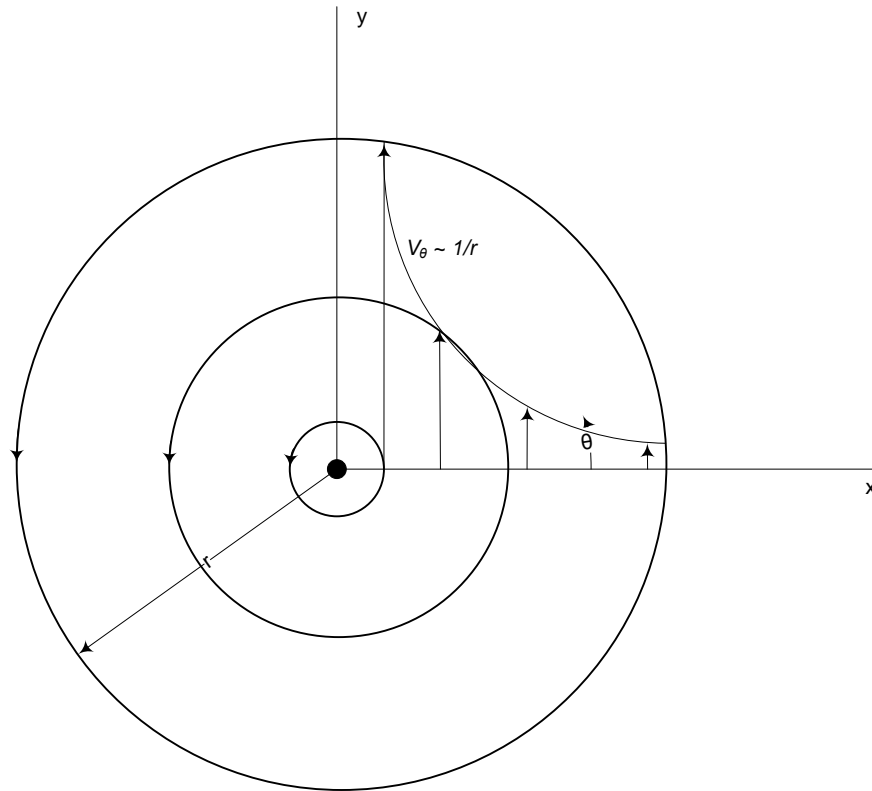
Figure 8 - Irrotational Vortex

Introducing circulation, Γ, which is defined as the line integral of the tangential component around a closed curve:

$$\Gamma = \oint_0^{2\pi} \frac{k}{r}(rd\theta) = 2\pi k \tag{27}$$

The velocity potential can be written as

$$\phi = \frac{\Gamma}{2\pi}\theta \tag{28}$$

A discontinuous surface is added to the computational plane that extends along the x-axis from the end of the wing to infinity resulting from vortex element of strength $-\Gamma$ at $(X_0, 0)$ as well as a counter vortex at $\left(\frac{1}{X_0}, 0\right)$ of strength Γ representing the circulation around the flat plate (see Figure 9). The counter vortex [added at $\left(\frac{1}{X_0}, 0\right)$] is added to ensure that Kelvin's circulation theorem is maintained in the system (i.e. there is no net circulation in the system).
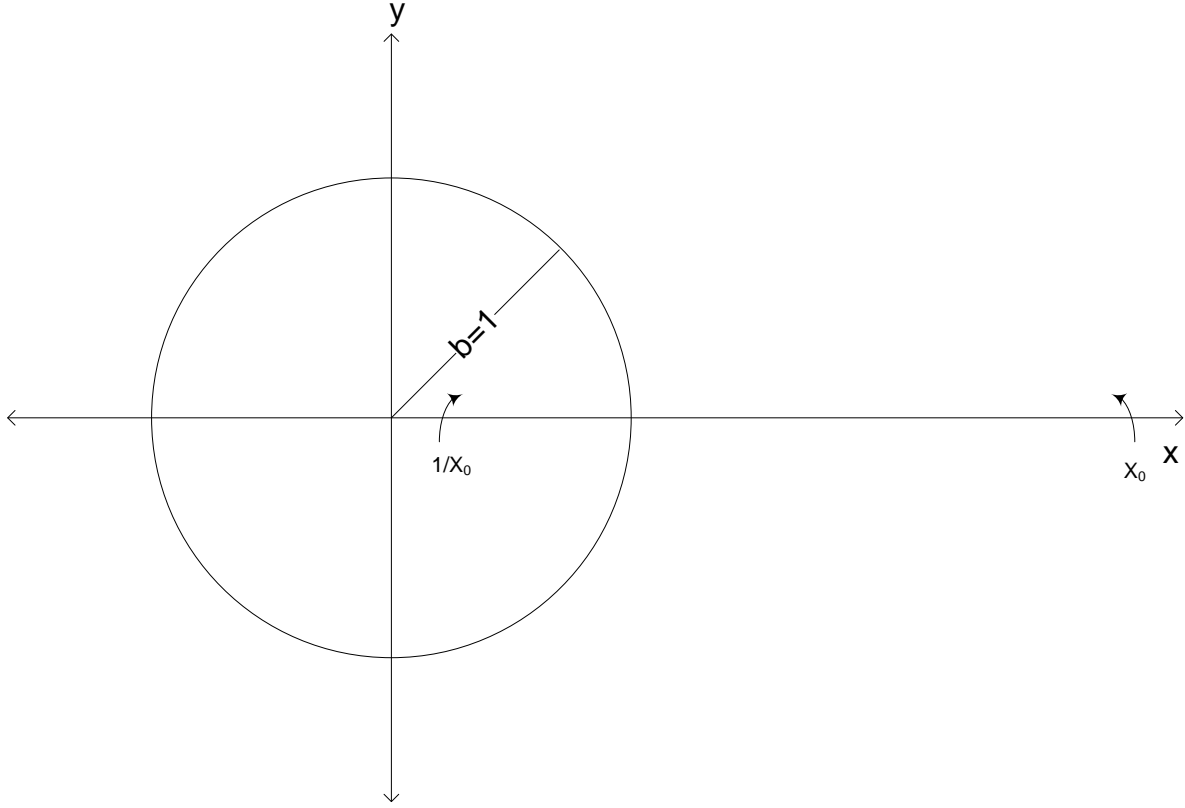
Figure 9 - Vortices in the Computational Domain

The angles formed between a point in the computational plane (x, y) and the two vortices $(X_0, 0)$

and $(\frac{1}{X_0}, 0)$ are

$$
\begin{aligned}
\theta_1 &= \arctan(\frac{y}{x - X_0}) \\
\theta_2 &= \arctan(\frac{y}{x - \frac{1}{X_0}})
\end{aligned}
\tag{29}
$$

Equation 28 can be rewritten to account for both vortices as

$$
\phi_\Gamma = \frac{\Gamma}{2\pi}[\arctan \frac{y(\frac{-1}{X_0} + X_0)}{x^2 - x(X_0 + \frac{1}{X_0}) + y^2 + 1}]
\tag{30}
$$

15

where ϕ_Γ is the flow potential due to the circulation. Introducing the following relation simplifies equation 30 to a form that can be reduced to eliminate the improper fraction from the equation and allows for an easier solution.

$$X_0 + \frac{1}{X_0} = 2x_0 \tag{31}$$

Noting that of interest is the potential along the surface so the substitution of equation (12 is made allowing equation 30 to be reduced to

$$\phi_\Gamma = \frac{-\Gamma}{2\pi} \arctan \frac{\sqrt{1 - x^2}\sqrt{x_0^2 - 1}}{1 - x \cdot x_0} \tag{32}$$

Equation 32 gives the clockwise circulation around the airfoil due to the circulation at point x_0.

Since the vortex center is moving away from the airfoil with a velocity u, the change in the velocity potential over time $\left(\frac{\partial \phi}{\partial t}\right)$ can be rewritten in terms of the centers of the vortices and the flow velocity:

$$\frac{\partial \phi}{\partial t} = \frac{\partial \phi}{\partial x_0} u \tag{33}$$

Recalling equation 22 the force due to the pressure arising from the circulation can be calculated by taking the derivative of equation 32 with respect to x:

$$\frac{\partial \phi_\Gamma}{\partial x} = \frac{\Gamma}{2\pi} \frac{\sqrt{x_0^2 - 1}}{(x_0 - x)\sqrt{1 - x^2}} \tag{34}$$

Also with respect to x_0:

$$\frac{\partial \phi_\Gamma}{\partial x_0} = \frac{\Gamma}{2\pi} \frac{\sqrt{1 - x^2}}{(x_0 - x)\sqrt{x_0^2 - 1}} \tag{35}$$

16

Substituting equation 33 into equation 22 gives

$$\triangle p = -2\rho u \left(\frac{\partial \phi}{\partial x} + \frac{\partial \phi}{\partial x_0} \right) \tag{36}$$

Substituting into this equations 34 and 35 and reducing gives

$$\triangle p = -2\rho u \frac{\Gamma}{2\pi} \frac{x_0 + x}{\sqrt{1 - x^2}\sqrt{x_0^2 - 1}} \tag{37}$$

To obtain the force, the pressure difference is integrated with respect to x over the entire flat plate:

$$L = \int_{-b}^{b} \triangle p = -\rho u b \Gamma \frac{x_0}{\sqrt{x_0^2 - 1}} \tag{38}$$

Defining Γ as

$$\Gamma = U dx_0 \tag{39}$$

where U is a function of a function of the of the distance from the location of the first vortex element to the flatplate or

$$U = f(ut - x_0) \tag{40}$$

and then integrating from the end of the flat plate to infinity to capture the effects of an infinitely extending circulatory wake gives:

$$L = -\rho u b \int_{1}^{\infty} \frac{U x_0}{\sqrt{x_0^2 - 1}} dx_0 \tag{41}$$

17

4. Determination of the Circulation Magnitude by the Kutta Condition

The magnitude, U, of the circulation is found by applying the Kutta condition which states that

the velocity at the trailing edge is not infinite (mathematically pinning the stagnation point to the

trailing edge) or

$$\frac{\partial}{\partial x}(\phi_\Gamma + \phi_\alpha) = 0 \tag{42}$$

at the trailing edge. Substituting into equation 42 the values for ϕ_Γ (equation 34) and ϕ_α

(equation 23) gives

$$\frac{\Gamma}{2\pi}\frac{\sqrt{x_0^2 - 1}}{(x_0 - x)} = xu\alpha b \tag{43}$$

Substituting in equation 39, then evaluating at $x = b$ gives

$$\frac{1}{2\pi}\int_1^\infty \sqrt{\frac{x_0 + 1}{(x_0 - 1)}}U dx_0 = u\alpha \tag{44}$$

Equation 41 is multiplied by 1 in a form derived from equation 42:

$$1 = \frac{u\alpha}{\frac{1}{2\pi}\int_1^\infty \sqrt{\frac{x_0+1}{(x_0-1)}}U dx_0} \tag{45}$$

To get a new form of equation 41:

$$L = -2\pi b\rho u^2 \alpha \frac{\int_1^\infty \frac{Ux_0}{\sqrt{x_0^2-1}}dx_0}{\int_1^\infty \sqrt{\frac{x_0+1}{(x_0-1)}}U dx_0} \tag{46}$$

To simplify the presentation of equation 46 the following substitution is made:

18

$$C = \frac{\int_1^\infty \frac{U x_0}{\sqrt{x_0^2-1}} dx_0}{\int_1^\infty \sqrt{\frac{x_0+1}{(x_0-1)}} U dx_0} \tag{47}$$

And equation 46 simplifies down to

$$L = -2\pi \mathrm{b} \rho u^2 \alpha C \tag{48}$$

Next we will evaluate parameter C. First, we write U in terms of a physical parameter.

$$U = U_0 e^{i \cdot k(\frac{\delta}{\mathrm{b}} - x_0)} \tag{49}$$

where $\delta = ut$ $(\delta \to \infty$ as $t \to \infty)$, and represents the distance between the flatplate and the

first vortex element and k (the reduced frequency) is a physical parameter describing the wave

length defined as

$$k = \frac{\omega \mathrm{b}}{u_0} \tag{50}$$

Substituting equation 49 into the equation 47 we have

$$C(k) = \frac{\int_1^\infty \frac{x_0}{\sqrt{x_0^2-1}} e^{-i \cdot k x_0} dx_0}{\int_1^\infty \sqrt{\frac{x_0+1}{(x_0-1)}} e^{-i \cdot k x_0} dx_0} \tag{51}$$

From this reduced form for $C(k)$ the integral can be solved by applying the Bessel equations to it.

The solution has the form $C(k) = F(k) + i \cdot G(k)$ where

$$F(k) = \frac{J_1(k)(J_1(k) + Y_0(k)) + Y_1(k)(Y_1(k) - J_0(k))}{(J_1(k) + Y_0(k))^2 + (Y_1(k) - J_o(k))^2} \tag{52}$$

and G is

$$G(k) = \frac{J_1(k)J_0(k) + Y_1(k)Y_0(k)}{(J_1(k) + Y_0(k))^2 + (Y_1(k) - J_0(k))^2} \tag{53}$$

The values of F and G are plotted in Figure 10 against *k*.
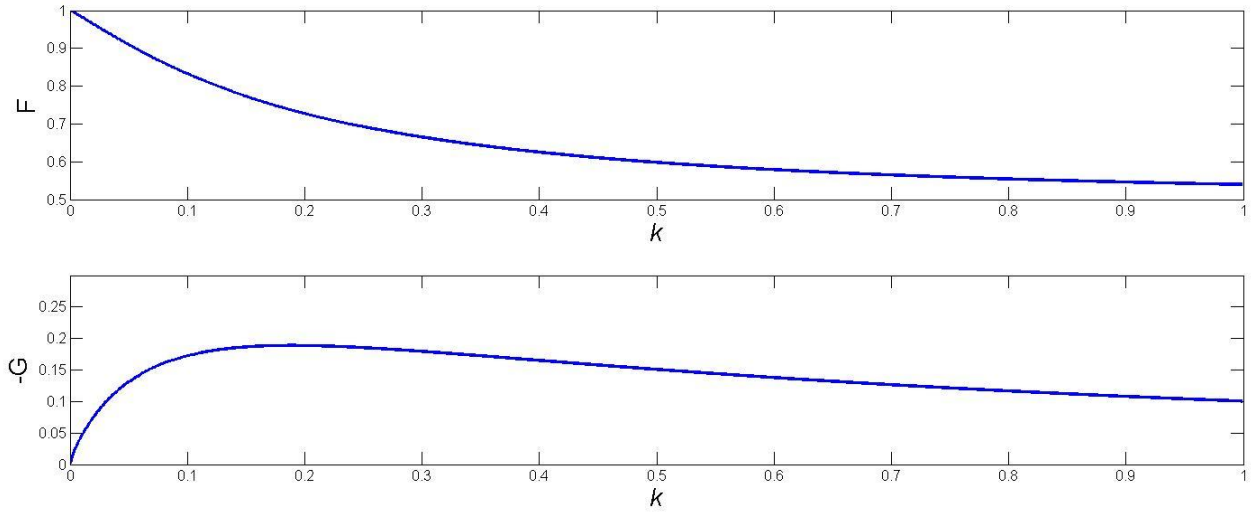
Figure 10 - Graph of F and -G against 1/*k*

6. Formulation of the Lift Equation in Unsteady Flow

To generate the equation for the lift on a flat plate in an oscillatory flow, the sum of the equations derived above (equations 25 and 48) is taken

$$L = \frac{-\pi}{2}\dot{u}\alpha b^2 + -2\pi b\rho u^2 \alpha C \tag{54}$$

and the flow velocity is the real portion of

$$u = u_0(1 - ia_u e^{i\omega t}) \tag{55}$$

where u_0 is the mean velocity, a_u is the fractional amplitude of flow velocity fluctuation, ω is the frequency of the wind gusts, and t is time. Substituting equation 55 into equation 48 gives

$$L = -\pi b\rho u_0 \alpha (\frac{b}{2}\omega Real((e^{i\omega t}) + u_0 Real((1 - ia_u e^{i\omega t}) \cdot C(k)) \cdot Real(1 - ia_u e^{i\omega t}) \tag{56}$$

The lift from a non-oscillatory flow is noted by setting

$$\begin{aligned} u &= u_0 \\ \dot{u} &= 0 \\ k &= 0 \\ C(k) &= 1 \end{aligned} \tag{57}$$

Substitution into equation 54 gives the non-oscillatory lift (L_0) as

$$L_0 = -2\pi b\rho u_0^2 \alpha \tag{58}$$

Equation 56 is then simplified and the substitution of $C(k) = F + i \cdot G$ is made

$$\frac{L}{L_0} = \frac{b\omega}{2u_0}a_u\left(Real(e^{i\omega t})\right) + Real((F + i \cdot G)(1 - ia_u e^{i\omega t}))Real(1 - ie^{i\omega t}) \tag{59}$$

The trigonometric form of the exponential is substituted into this equation and expanded and then reduced using trigonometric identities

21

$$\frac{L}{L_0} = (1 + \frac{a_u^2 F}{2}) + a_u(\frac{k}{2} + G)\cos\omega t + a_u(1 + F)\sin\omega t - \frac{a_u^2 F}{2}\cos 2\omega t + \frac{a_u^2 G}{2}\sin 2\omega t \quad (60)$$

From the final form of equation 60, the time dependent lift force due to an oscillating freestream can be identified as well as the average lift over an entire gust cycle is

$$\bar{L} = L_0(1 + \frac{a_u^2 F}{2}) \quad (61)$$

Previous experimental research papers looking at the effects of unsteady flow on the lift force have been published by Williams et al. (2009a, b).

1.   Experimental Setup

The experiments were performed by Williams et al. in a wind tunnel modified by the addition of shutters to be able to approximate a sinusoidal input for the freestream velocity. Figure 11 shows the layout of the wind tunnel.
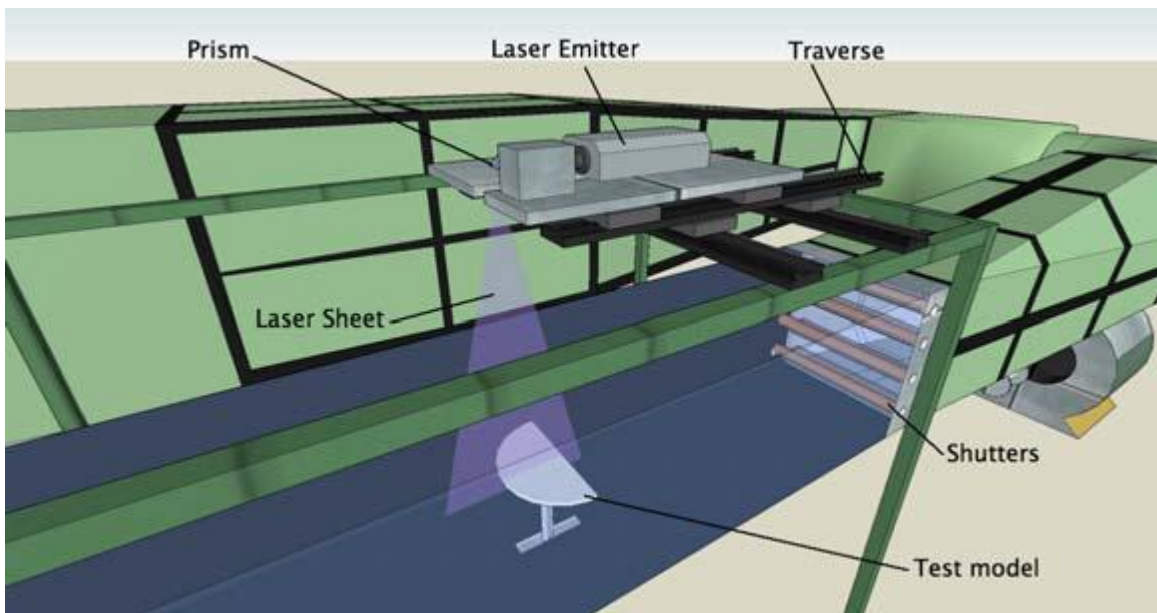
Figure 11 - Wind Tunnel Setup Used by Williams et al. (2009a, b)

The model is a semicircular wing with an aspect ratio of 2.54. The experimental setup could generate chord based mean Reynolds numbers between 40,000 and 71,000. The shutters where controlled via a computer and could be operated up to a frequency of 3Hz. The amplitude of the freestream variation that could be obtained with this setup was in the range of three to ten percent of the mean freestream velocity.

2.   Experimental Results

The principle objective of their work was to implement a control scheme intended to suppress oscillations in the lift amplitude due to the oscillations in the freestream velocity. Of concern to this thesis are their results detailing the peak-to-peak amplitude in the lift force as well as the phase between the lift and the flow stream. Figure 12 shows their experimental results versus the theoretical model which was derived above. The results were from experiments run with a variation in the freestream of 3.33%.
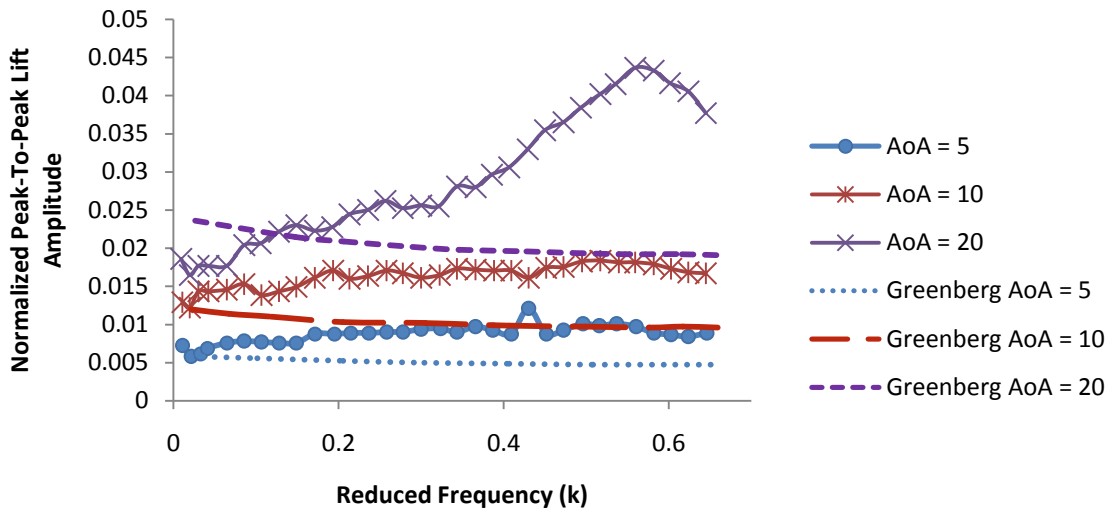
Figure 12 - Peak-to-Peak Lift Amplitude (Williams et al. 2009b)

From Figure 12 it can be seen that there is a large discrepancy between the experimental observations and what the theoretical model was predicting. In some cases, the theoretical model under predicted the experimental results by close to 100%. This gives evidence that the theoretical model is ill-equipped to be used to predict the flight characteristics of an airfoil in an oscillating flow stream.

Williams et al. (2009a) reported the experimental phase between the measured lift and the flow stream and compared this to the theoretical model, as in Figure 13.
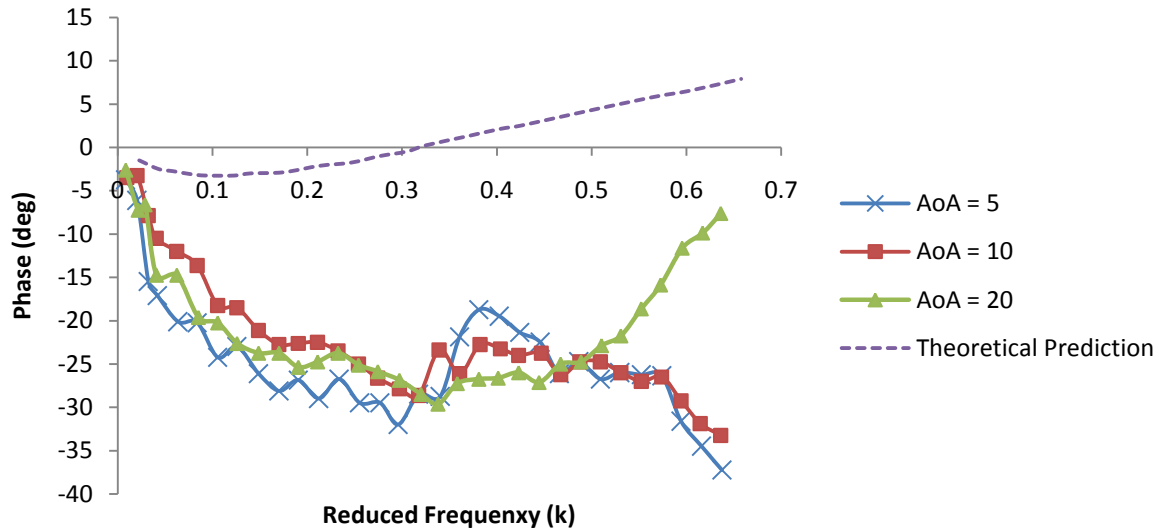
Figure 13 - Phase between Lift and Flowstream (Williams et al., 2009a)

The phase from the experimental data and the theoretical model differ greatly which indicates the theoretical model may be inadequate when predicting the phase between the lift response and the flow stream (measured input). Being able to accurately predict the phase becomes important if any sort of control mechanism is implemented. Using theoretically predicted phase instead of the experimentally derived phase can lead to improper control implementation which can reduce the effectiveness and in some extreme cases compound the variation rather than reducing it.

D. Motivations

The size and weight restrictions of MAVs impose limits to the size and complexity of the components it can carry. This limit the size of the power source it can carry affecting the flight duration and consequently the effective range. Previous studies (Lissaman, 2005, Patel, 2006, Langelaan and Bramesfeld, 2008, and Lissaman and Patel, 2007) have established the benefits of wind gusts in extending the flight duration and this thesis hopes to provide data that can be used to help optimize the methods of energy extraction from gusts while minimizing path deviations.

The instrumentation limitations necessitate an emphasis on maintaining a steady position, especially in the cases of camera usage where vertical variations would be detrimental to the footage being obtained, because the size and sophistication of the instruments are limited by what the MAV can carry leading to an impact on the achievable clarity of measurements/recordings. This thesis hopes to provide data to accurately reflect the variations in the lift force generation over a gust period and how the nature of the gust affects the lift response.

While the theoretical models can evaluate the response of a flat plate to an oscillatory flow, previous studies have shown there is disagreement between experimental results and theoretical predictions in both the peak-to-peak amplitude of the lift response and the phase between the flow stream and the lift response. These previous experiments have been performed at Reynolds numbers of approximately 50,000, whereas MAV operation in a much low Reynolds number region. Additionally, previous experimental work was limited by the variation in the flow speed it could create; a limit below what is normally would be seen in real world applications. The numerical study isn't limited by the amplitude of the variations achievable and

26

as such can better reflect the real world response that an MAV might experience, with these results the detrimental effects of oscillating flow can be minimized while the positive benefits can be better optimized

II.   NUMERICAL METHOD

A. <u>Navier-Stokes Equations</u>

This chapter discusses the equations which govern the physical phenomena that are simulated; it starts with the general equations and adapts them to model incompressible viscous flow. The study was performed in a 2-dimensional plane so the equations are limited to their 2-D form.

The equations which model fluid flow are derived from the equations that model conservation of mass and momentum (Munson et al., 2006). The continuity equation which shows the time rate of change of the mass of a system is given by

$$\frac{\partial}{\partial t} \int_{cv} \rho dV + \int_{cs} \rho \vec{u} \cdot \hat{n} dA = 0 \tag{62}$$

The continuity equation states that to conserve mass, the time rate of change of the mass of the matter inside a control volume plus the net rate of flow of mass through the control surface must be equal to zero. The continuity equation expressed in differential vector form is

$$\frac{\partial \rho}{\partial t} + \nabla \cdot (\rho \vec{u}) = 0 \tag{63}$$

The equations of motion are derived from Newton's second law of motion applied to a differential element:

$$\begin{aligned} \delta F_x &= \delta m \cdot a_x \\ \delta F_y &= \delta m \cdot a_y \end{aligned} \tag{64}$$

Substituting the surface and body forces acting on the differential elements yields the following for the momentum equation:

$$\rho g_x + \frac{\partial \sigma_{xx}}{\partial x} + \frac{\partial \tau_{yx}}{\partial y} = \rho(\frac{\partial u}{\partial t} + u\frac{\partial u}{\partial x} + v\frac{\partial u}{\partial y})$$
$$\rho g_y + \frac{\partial \tau_{xy}}{\partial y} + \frac{\partial \sigma_{yy}}{\partial y} = \rho(\frac{\partial v}{\partial t} + u\frac{\partial v}{\partial x} + v\frac{\partial v}{\partial y}) \tag{65}$$

The equations of motion are transformed into the form of Euler's equations of motion by making

the substitution of pressure for the negative normal stress or

$$-p = \sigma_{xx} = \sigma_{yy} \tag{66}$$

The substitution can be expressed in vector notation as

$$\rho g - \nabla p = \rho\left(\frac{\partial \vec{u}}{\partial t} + (\vec{u} \cdot \nabla)\vec{u}\right) \tag{67}$$

For this study the gravitational forces are neglected and the viscous terms $\sigma_{xx,yy}, \tau_{xy}$ can be

defined as follows:

$$\sigma_{xx} = 2\mu(\frac{\partial u}{\partial x}) \tag{68}$$

$$\sigma_{yy} = 2\mu(\frac{\partial v}{\partial y}) \tag{69}$$

$$\tau_{xy} = \mu(\frac{\partial u}{\partial y} + \frac{\partial v}{\partial x}) \tag{70}$$

For incompressible flow equations 63 and 67 can be simplified to two equations

(Tannehil et al. 1997)

$$\nabla \cdot \vec{u} = 0 \tag{71}$$

$$\frac{\partial (\vec{u})}{\partial t} + \vec{u} \nabla \cdot (\vec{u} \cdot \vec{u}) = \frac{-\nabla p}{\rho} + v \nabla^2 \vec{u} \tag{72}$$

where v is the kinematic viscosity.

Equations 71 and 72 are non-dimensionalized wherein the values are normalized to fall between zero and one and the equations are independent of the system of units used. The system is normalized by the Reynolds number:

$$\bigtriangledown \cdot \vec{u} = 0 \tag{73}$$

$$\frac{\partial(\vec{u})}{\partial t} + \vec{u} \bigtriangledown \cdot (\vec{u} \cdot \vec{u}) = -\bigtriangledown p + \frac{1}{\mathrm{Re_L}} \bigtriangledown^2 \vec{u} \tag{74}$$

where $\mathrm{Re_L}$ is the Reynolds number based on the normalized freestream density ρ_∞, velocity U_∞, viscosity μ_∞, and reference length it is calculated by

$$\mathrm{Re_L} = \frac{\rho_\infty u_\infty L}{\mu_\infty} \tag{75}$$

Equations 71 and 72 can be expanded into 2-D Cartesian coordinates which form the basis for a lot of the numerical models solving the incompressible Navier-Stokes equations (Tannehill et al., 1997):

$$\frac{\partial u}{\partial x} + \frac{\partial v}{\partial y} = 0 \tag{76}$$

$$\frac{\partial u}{\partial t} + u\frac{\partial u}{\partial x} + v\frac{\partial u}{\partial y} = -\frac{\partial p}{\partial x} + \frac{1}{Re_L}\left(\frac{\partial^2 u}{\partial x^2} + \frac{\partial^2 u}{\partial y^2}\right) \tag{77}$$

$$\frac{\partial v}{\partial t} + u\frac{\partial v}{\partial x} + v\frac{\partial v}{\partial y} = -\frac{\partial p}{\partial y} + \frac{1}{Re_L}\left(\frac{\partial^2 v}{\partial x^2} + \frac{\partial^2 v}{\partial y^2}\right) \tag{78}$$

Equations 76-78 are the normalized forms of the equations needed to solve the 2D Navier-stokes equation in a Cartesian coordinate system.

30

B. Solving the Incompressible Navier-Stokes Equations

Presented in this section is the numerical method used to solve the governing equations (Henshaw, Kreiss, and Reyna., 1994). The initial boundary value problem (IBVP) for equations 73 and 74 are

$$\bigtriangledown \cdot \vec{u} = 0 \qquad for \quad x \in D, t > 0 \tag{79}$$

$$\frac{\partial(\vec{u})}{\partial t} + \vec{u} \bigtriangledown \cdot(\vec{u} \cdot \vec{u}) = \frac{-\bigtriangledown p}{\rho} + \upsilon \bigtriangledown^2 \vec{u} \qquad for \quad x \in D, t > 0 \tag{80}$$

with the initial conditions and boundary conditions (as defined by the user)

$$\vec{u}(\vec{x}, t) = \vec{u_0}(\vec{x}) \qquad for \quad x \in D, t_0 = 0 \tag{81}$$

$$B(\vec{u}, p) = g \qquad for \quad x \in \partial D, t \geq 0 \tag{82}$$

where $\vec{x}$ contains the Cartesian coordinates (x, y) in the physical domain P, the vector $\vec{u}$ contains the Cartesian velocities $(\vec{u}, \vec{v})$, D is a bounded domain $P \in R^N$ (where N=1,2,3…), ∂D is the boundary of the domain D, t is time, p is the pressure, ρ is density, υ is the kinematic viscosity, B is the boundary condition, g is the boundary data, and $\vec{u_0}$ is the initial velocities. From these equations, an alternative system of equations can be developed, referred to as the velocity-pressure formulation (Henshaw 1994), that allows for the solution of the pressure field by introducing the following equation and boundary condition

$$\frac{\bigtriangledown^2 p}{\rho} + \bigtriangledown u \cdot \vec{u_x} + \bigtriangledown v \cdot \vec{u_v} = 0 \qquad for \quad x \in D, t > 0 \tag{83}$$

$$\bigtriangledown \cdot \vec{u} = 0 \qquad for \quad x \in \partial D, t > 0 \tag{84}$$

Using equations 83 and 84 a numerical solution can be calculated using the boundary and initial conditions in equations 81, 82, and 84. From equation 83 (commonly called the pressure-Poisson equation, PPE), the pressure can be calculated if the velocity field is known. However

the lack of an explicit boundary with the PPE prevents the use of this in a numerical method. To

get around this limitation the momentum equation is modified by use of the normal component,

$\hat{n}$:

$$\frac{\partial p}{\partial \hat{n}} = \hat{n} \cdot (-\vec{u}_t - (\vec{u} \cdot \bigtriangledown)\vec{u} + \upsilon \bigtriangledown^2 \vec{u})\rho \qquad for \quad x \in \partial D, t > 0 \tag{85}$$

To minimize divergence due to truncation errors and interpolation errors, a divergence term is

added to equation 83 that is in the form α_{dc} where the artificial diffusion is comprised of a

number of the magnitude of the square of the local grid size. For a good simulation the artificial

diffusion must be large enough so the smallest significant features show up in the mesh, but

small enough that the variation in the system isn't dampened out. The new equation with the

artificial diffusion is

$$\frac{\bigtriangledown^2 p}{\rho} + \bigtriangledown u \cdot \vec{u_x} + \bigtriangledown v \cdot \vec{u_v} - \alpha_{dc} \bigtriangledown \cdot \vec{u} = 0 \qquad for \quad x \in D, t > 0 \tag{86}$$

The equations are discretized using the second order centered finite difference approximation

method and the resulting system of equations can be expressed as

$$\frac{d\vec{u}}{dt} = F(\vec{u}, p, t) \tag{87}$$

The velocity field is solved from equation 86 or from an initial value. To keep the velocity and

pressure equations decoupled, a time stepping scheme, called the split-step scheme, is employed.

The equations are solved using a semi-implicit multistep method using a Crank-Nicolson scheme

for the viscous terms and a second order Adams-Bashforth predictor-corrector for the convective

and pressure terms (Henshaw and Peterson 2001).

III.   GRID GENERATION AND SENSITIVITY ANALYSIS

This section details the layout of the grid used for the numerical simulations and the grid sensitivity analysis that was performed to ensure the accuracy of the results from the simulations performed.

A. Grid Layout

The general layout for the grid can be seen in Figure 14. The grid layout consists of three different grids the background grid, the trailing grid, and the body fitted grid. In this layout, the background, and trailing grids are Cartesian grids, and the grid around the object is a body fitted grid. The usage of the three different grids allowed for an optimized computational speed for the numerical simulations. Each grid has a different level of refinement with the background grid being the coarsest. The flow field can be better resolved with the trailing grid in an efficient manner. Compared to a setup without the trailing grid the area that the body fitted grid occupies would need to be larger to have the same accuracy in the results. In instances where there is a large discrepancy between the sizes of cells at the overlapping region there is a computational error resulting from a large number of cells pulling data from the same interpolation point. To avoid this error, the background grid is stretched in a way that clusters more points in the center near where the body fitted and trailing grid are located.
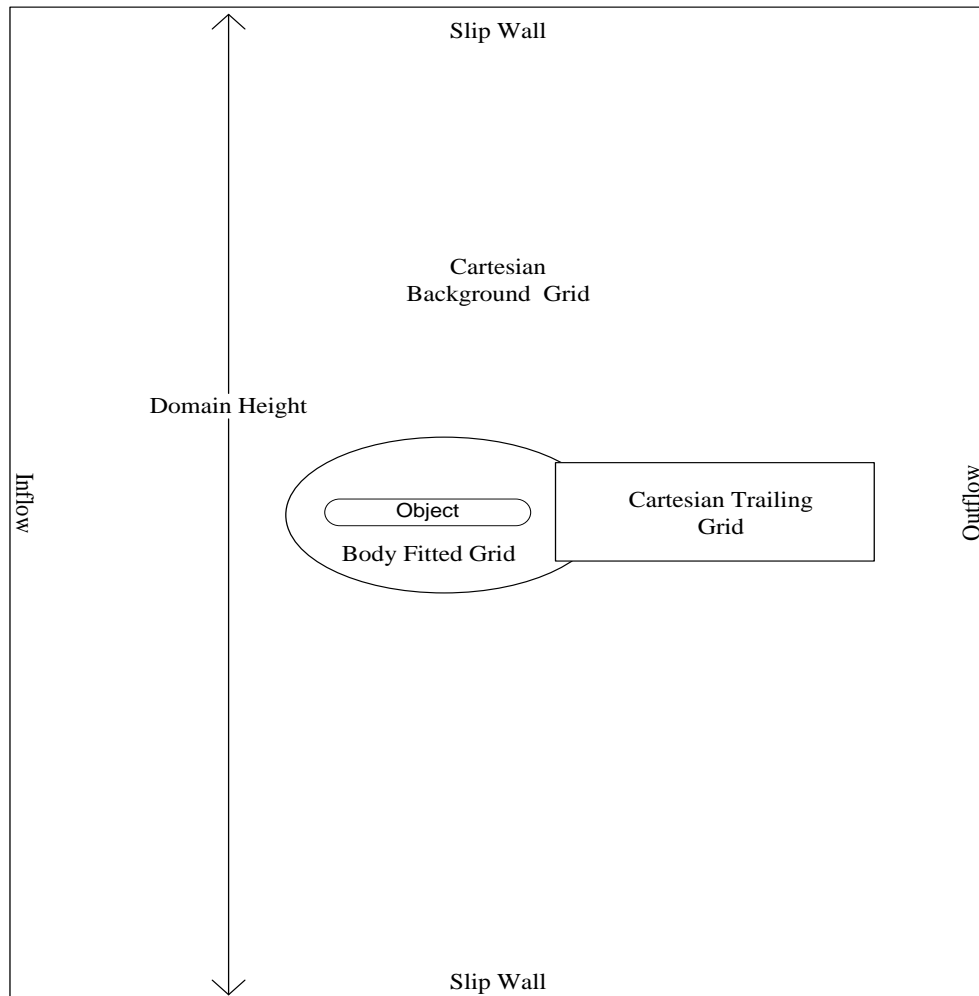
Figure 14 - Diagram for the Grid Layout

The body fitted grid is a hyperbolically mapped structured grid around a flat plate. The hyperbolic grid is generated by mapping a grid to a specified curve by marching around the given curve using a backward Euler method then the generating cells outward radially. To minimize computational error the ratio between the cell size of the body fitted grid and the trailing grid was kept close to 1:1 in the overlapping regions. The body fitted grid was stretched to cluster more grid points close to the airfoil to capture the boundary layer. Clustering grid

points close to the surface allows the grid to capture these changes accurately in the boundary

layer.

B. Grid Sensitivity Analysis

Sensitivity analysis was performed to ensure the solutions are grid independent. The results for the sensitivity analysis are given in terms of the number of cells outward radially, NR, and along the circumference, NT. The number of cells in the other grids are then based off of various ratios to the body fitted grid. The grids were tested at a Reynolds number of 1000. The simulations were run to a point where the lift history converged or reached a periodic behavior. The coefficients were averaged based on the converged or periodic forces. The sensitivity analysis results are given in Table I.

Cells in Radial Direction, NR	Cells in Circumferential Direction, NT.				
	NT = 100	NT = 150	NT = 200	NT = 300	NT = 400
NR = 50	0.49552	0.48723	0.48723	0.48829	0.48867
NR = 100	0.50469	0.50469	0.50469	0.50883	0.50883
NR = 150	0.52178	0.51400	0.50861	0.50883	0.50872

Table I
SENSITIVITY TEST FOR GRID SETUPS

As the number of points in the circumferential direction, NT, is increased beyond 100, the lift does not show much variation with the number of points in the radial direction, NR. When NR is larger than 100, increasing the number of points in radial direction, NR, from 50 to 100 can significantly increase the lift coefficient; a further increase of NR leads to less than 0.5% change in the calculated lift force. From the analysis a grid of NR=100 and NT=100 is chosen.

IV.   NUMERICAL RESULTS

This section details the results of the numerical study of the effect of an oscillating flow stream on a flat plate. The study focuses on 4 different aspects: the effect of the fluctuation amplitude of the freestream velocity on the cycle averaged lift, the effect of the reduced frequency on the cycle averaged lift, the effect of the reduced frequency on the peak-to-peak amplitude in the lift force and the effect of the reduced frequency on the phase between the lift response and the freestream velocity.

A.   Numerical Setup

The numerical analysis uses a single frequency harmonic longitudinal gust described by

$$u = u_0(1 + a_u \cdot \cos(2\pi f t)) \tag{88}$$

where u_0 is the mean freestream velocity, a_u is the amplitude of freestream oscillation, f is the frequency of the gust. For the simulations, the gust oscillation amplitude a_u is set as a decimal (for example 0.05 or 0.10) signifying gust amplitudes as a percentage of the mean freestream speed (from the example, either 5% or 10% of the freestream speed) and f is varied to achieve the various reduced frequencies. The Reynolds number based on the mean freestream velocity u_0 is 1000, which is a low range for MAV operation.

Lift coefficient versus the AoA is compared between experimental results (Williams et al. 2009b) and the numerical results in non oscillatory flow as a baseline validation of the numerical simulations. The numerical results were allowed to run until either a steady state (for angles of attack that do not exhibit flow separation) or a periodical force history (where flow separation is noted) was achieved (this occurred approximately 25 seconds into the simulation). The lift coefficient was calculated from the averaged force over the time when the solution was periodic.

From Figure 15, it can be seen that there is a reasonable agreement between the simulation and measurement. The simulation coincides with the measurement at lower angles of attack. At modest angles of attack, the experiment shows higher lift coefficient than the simulation. A clear stall is observed in the high Reynolds number measurement (Re= 56,000), but no stall occurs in the low Reynolds number simulation (Re=1000). This is consistent with the previous findings (Hord and Lian 2010) for flat plates in these Reynolds number ranges.
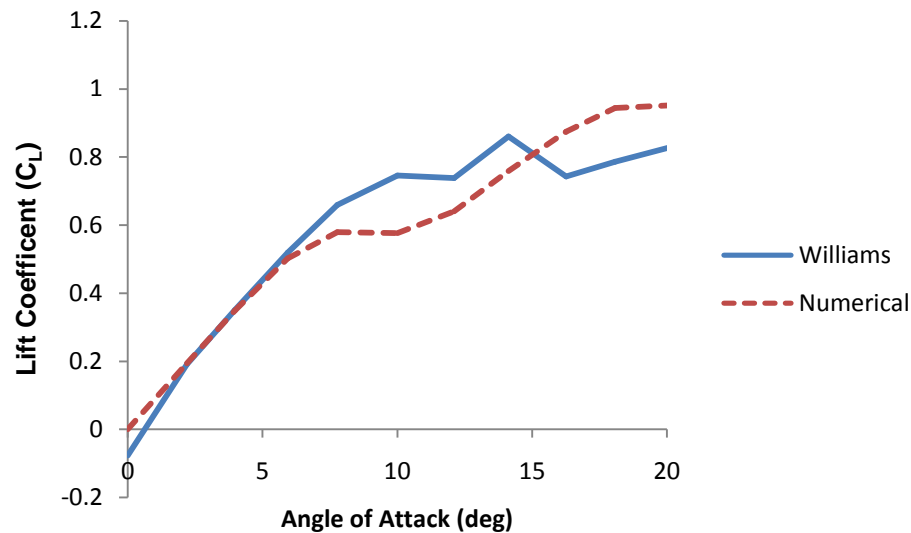
Figure 15 - Comparison of Lift Coefficient versus the AoA for a Flat Plate

In the following sections the results of the numerical simulations are compared with the theoretical prediction (hereafter referred to as Greenberg's theory) to determine the effect of the freestream oscillation amplitude on the force response.

Comparisons are also made with experiments (Williams et al. 2009b) performed at a much higher Reynolds number of 56,000 under oscillating flow cinditions. The experiment was run at a gust frequency of 3 Hz and an averaged mean flow speed of 4 m/s using a 0.243 meter

chord flat plate. To maintain the same reduced frequency *k* of 0.57, the numerical simulation is

run at a gust frequency of 0.18 Hz and a mean flow speed of 1 m/s using a 1 m chord flat plate;

both the simulation and experiment have an oscillation amplitude of 5% of the mean flow speed.

Figure 16 shows the computed lift over 2 gust periods as well as Greenberg's theoretical

predication. Here the lift is normalized by its time averaged value. The numerical lift history

presented is taken after periodic lift history is observed; but in the figure the starting time is

shifted to the origin, and this does not mean the first two cycles were reported). Both the

simulation and measurement predict a higher lift amplitude than the theoretical prediction and

there is a slight discrepancy among the phase shifts; however, despite the Reynolds number

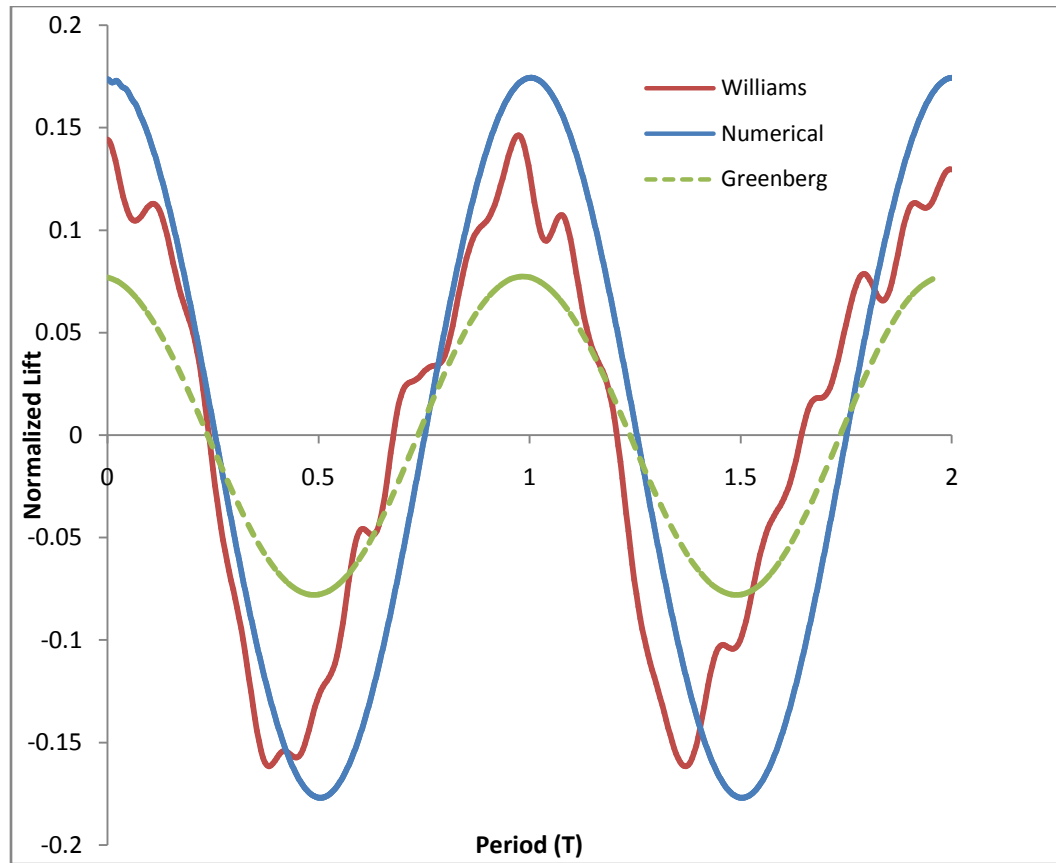difference, the three approaches show similar trend in the lift variation.

Figure 16 - Normalized lift history for an experimentally measured 3D flat plate and a numerically simulated 2D flat plate

B. Effect of the Freestream Oscillation Amplitude.

If a constant lift coefficient is assumed, then a quasi-steady analysis of equation 60 shows that the ratio of the lift in oscillating flow to the lift in steady flow (L_o) has a theoretical prediction:

$$\frac{L}{L_0} = (1 + \frac{a_u^2 F}{2}) + a_u(\frac{k}{2} + G)\cos\omega t + a_u(1 + F)\sin\omega t - \frac{a_u^2 F}{2}\cos 2\omega t + \frac{a_u^2 G}{2}\sin 2\omega t$$

An oscillating freestream was numerically simulated at two reduced frequencies, k, values for a 10º AoA. The amplitude was set as 5% and 10% of the freestream speed. Figure 17 shows the lift history normalized by the time averaged lift ($\frac{L}{L_0} - 1$) for 2 different k values along with Greenberg's approximation. At the lower reduced frequency of 0.162 (a reduced frequency a MAV might experience at flight speed), Greenberg's prediction matches up closely to the numerical simulation. At the higher reduced frequency of 0.315(a reduced frequency a MAV is likely to experience while gliding), the numerical result is higher than the theoretical value. At the lower reduced frequency, flow remains attached and no vortex shedding is observed. However, at the higher reduced frequency, flow separation and vortex shedding occur. The Greenberg theory is based on attached flow and may not be suitable for describing separated flows which occur at the higher reduced frequencies in the study. It's concluded that using the Greenberg theory at high reduced frequency to predict the flight response could be problematic. In real world terms, the predicted flight trajectory will show larger fluctuations in vertical position over a period than what would be expected using the theoretical predictions. In instances where maintaining a steady position is critical, such as recording video, taking measurements, or instrumented readings, these larger variations can be detrimental if they are not

accounted for and corrected. Additionally, knowing the specific lift variation may be required to

implement precision maneuvers.
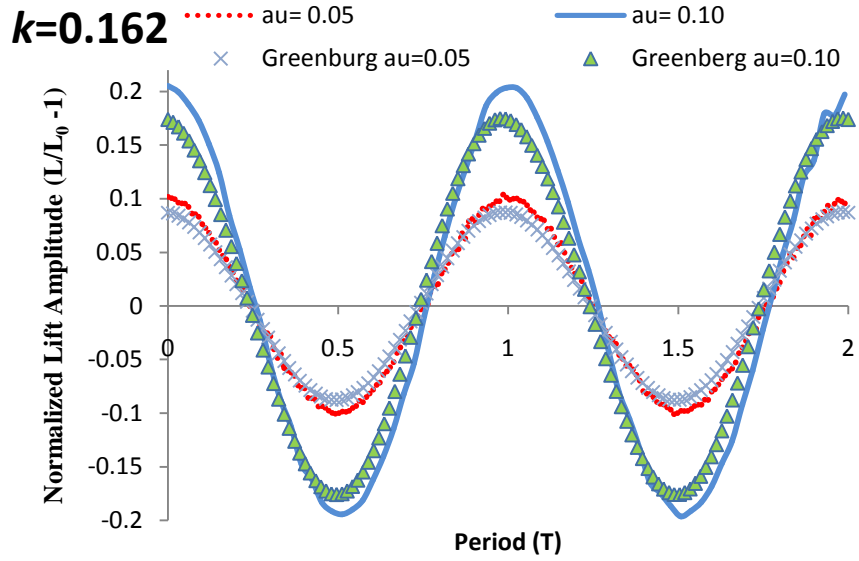
(a)
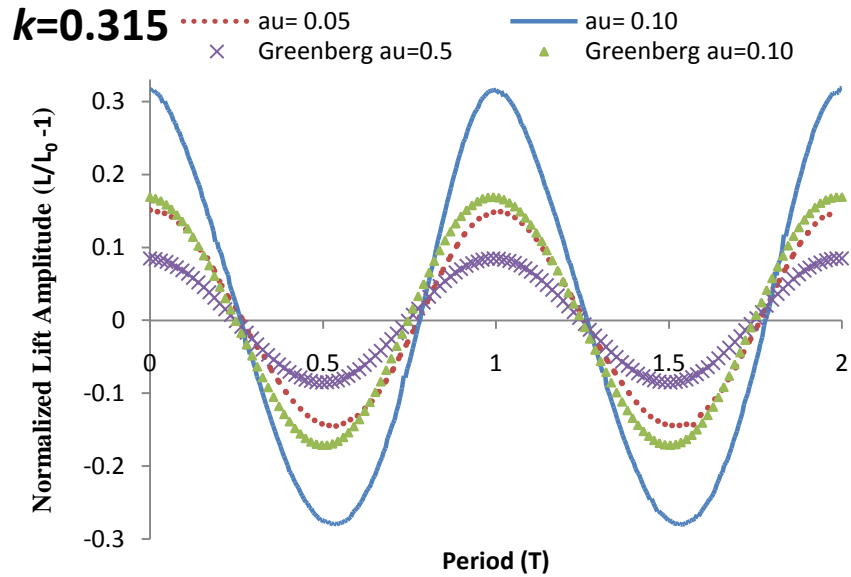
(b)

Figure 17 - Normalized lift at AoA of 10º over 2 periods for *k* value equal to 0.162(a) and 0.315 (b).

Under a quasi-steady assumption theoretical analysis shows that a wing generates a higher time averaged lift in an oscillating freestream than in a steady one. This was shown in equation 61

$$\bar{L} = L_0(1 + \frac{a_u^2 F}{2})$$

Based on the prior results, cases were run at a high reduced frequency knowing that the results would vary compared to the theoretical predication more than if a lower reduced frequency were used. The freestream amplitude was increased beyond the 10% used by Williams et al. to see how much variation there was between the numerical results and what was theoretically predicted. The simulations were run at a reduced frequency of 0.5, AoA of 10° and a Reynolds number of 1,000. For the analysis, the time averaged lift was normalized by the nominal lift under the identical AoA but with steady freestream. The results are shown in Figure 18.
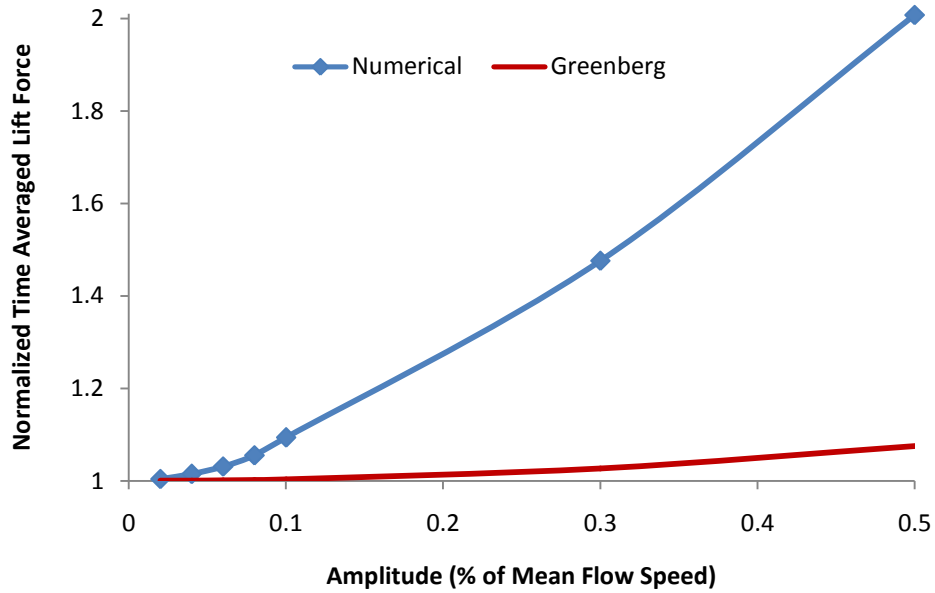
Figure 18 - Normalized Cycle Averaged Lift Force at AoA of 10°, *k* of 0.5 and Varying Freestream Oscillation Amplitudes

Like Greenberg's prediction, the numerical simulation suggests a quadratic relationship; however, the numerical results are much higher than Greenberg's theoretical prediction. A possible explanation for this is that the theoretical prediction is based on a constant lift coefficient. Previous studies (McMasters et al. 1980) have shown that the lift coefficient is dependent on the Reynolds number which makes the assumption of a constant lift coefficient invalid. Additionally, the high reduced frequency (*k*=0.5) leads to flow separation and vortex shedding, which violates the assumptions of Greenberg's theory.

C. Impact of Reduced Frequency on the Time Averaged Lift

From equation 61 it can be seen that in addition to the freestream amplitude the time averaged lift is also dependent on F which is a function of the frequency of the freestream oscillation.

$$\bar{L} = L_0 (1 + \frac{a_u^2 F}{2})$$

To investigate the impact of the frequency of the freestream oscillation on the time averaged lift, simulations were run at two AoA's, 6° and 10°, with a freestream oscillation amplitude of 10% of the freestream velocity. The frequency of the freestream oscillations was varied to achieve different reduced frequencies, and the resulting lift was averaged over one cycle and normalized by the lift in a non-oscillating freestream. Figure 19 shows the time averaged lift dependence on the reduced frequency as well as the values predicted by Greenberg's theory.
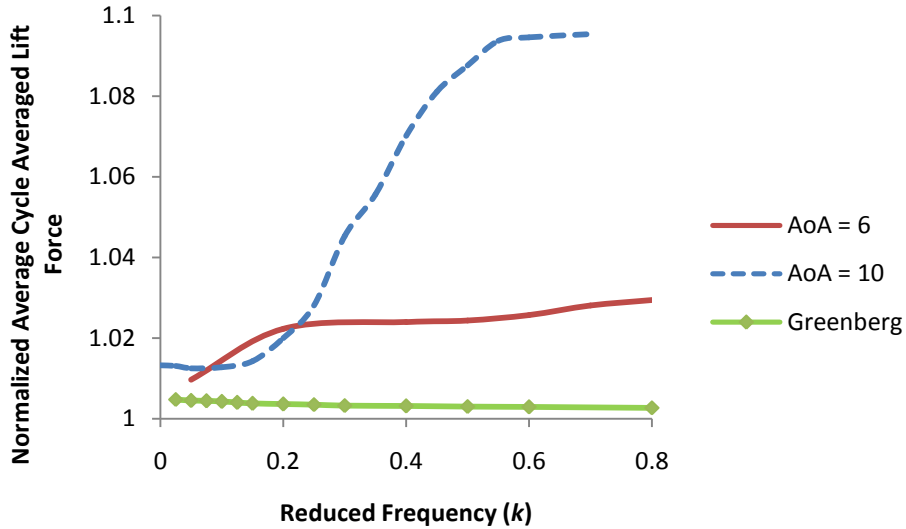

Figure 19 - Normalized Cycle Averaged Lift at AoAs 6° and 10° for various k values with a_u=0.10.

At both angles of attack there is an increase in the time averaged lift force as the reduced frequency increases. At 6º the increase is negligible; at 10º the average at a high k value is approximately 10% higher than that at a low k value. At both ends ($k<0.2$ and $k>0.55$), the averaged lift is almost flat. Although Greenberg's theory predicts the dependence of the averaged lift on the reduced frequency, it shows a much smaller variation than the simulation.

Figure 20 is a comparison between the lift histories at a high and a low k value for the 10º AoA and offers some insight into the differences in the averaged lift. The lift history at $k = 0.8$ is higher at all points when compared to the history at $k = 0.025$. Additionally, while the lower k value shows sinusoidal shape, the higher k value lift histories have a non-sinusoidal shape, indicating high non-linearity at the higher reduced frequency. At both reduced frequencies, Greenberg's theory shows a sinusoidal shape. In both cases, lift histories are plotted over one period after the simulations reach periodicity. In the figure, the origin represents the onset of the periodic lift not a simulation time of zero.
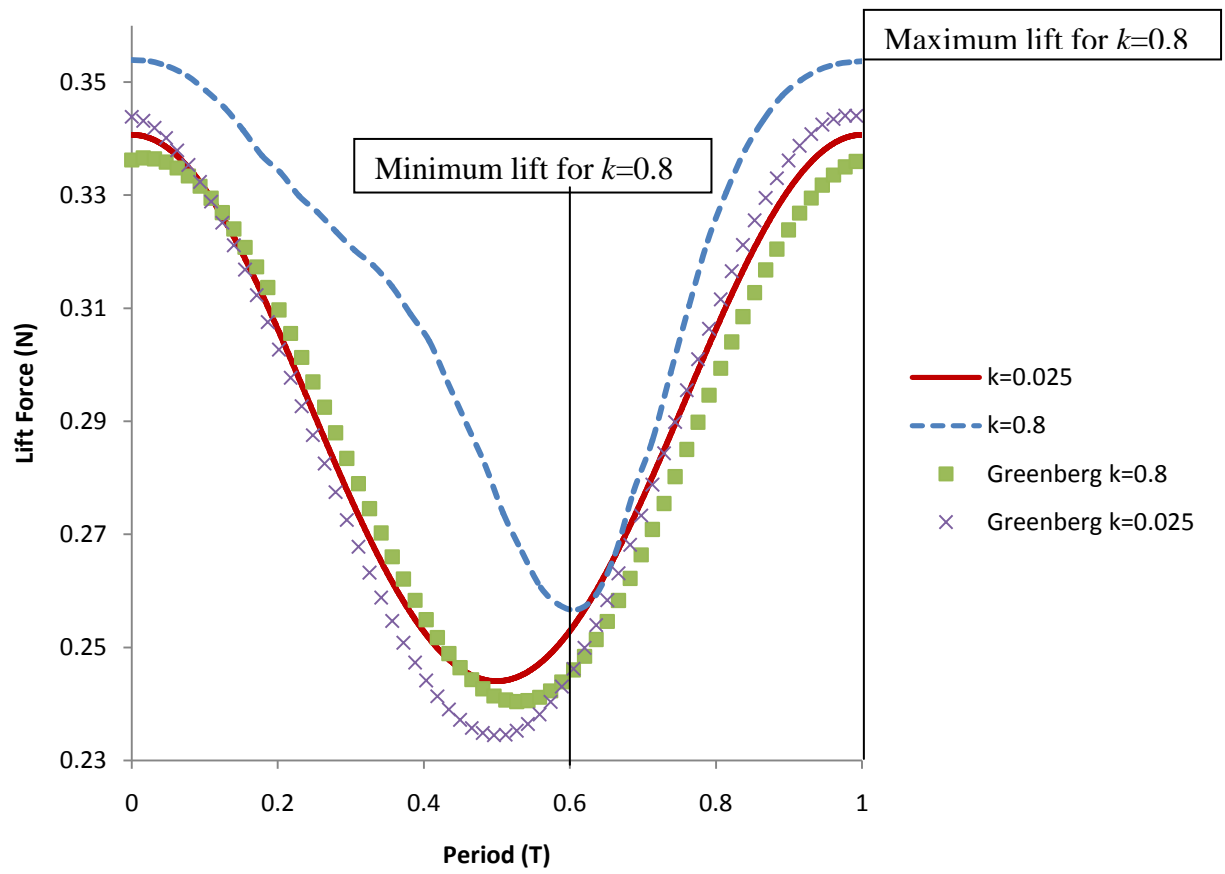
Figure 20 - Lift History over 1 Period for a 10° AoA at *k* = 0.025 and 0.8

D. Lift Oscillation Amplitude Dependence on the Reduced Frequency

The lift amplitude is important because it has a direct impact on the magnitude of the variation in the vertical position of a undergoing a lift history similar to the one simulated. In this study the lift amplitude is defined as the difference between the maximum lift (L_{max}) and time averaged lift (L), while the peak-to-peak lift amplitude is defined as the difference between the maximum lift (L_{max}) and the minimum lift (L_{min}). From Figure 20 the peak-to-peak amplitude for $k=0.8$ would be calculated as the difference between the values for the lift force a T=1 and T=0.6. Figure 21 shows the peak-to-peak lift amplitude, which is the normalized by the averaged lift and contains data for both the 6° and 10° cases. In both cases, the peak-to-peak lift amplitude increases with the reduced frequency. However, they peak at different k values. In addition, the 10° case shows a much larger variation than the 6° case.

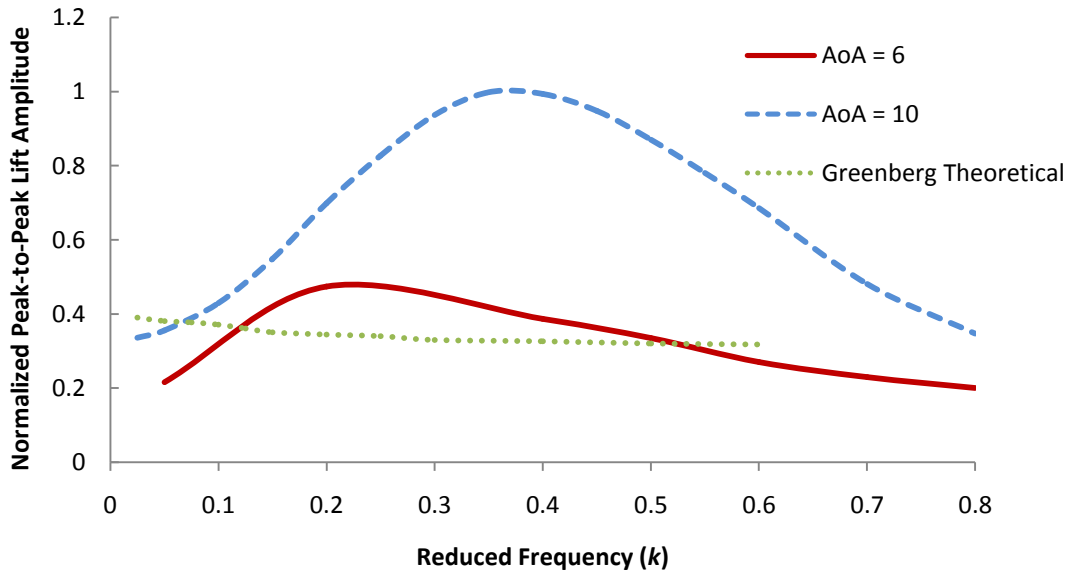**Figure 21 - Normalized Peak-to-Peak Lift Amplitude versus Reduced Frequency (k) for AoA = 6° and 10°.**

For the 6° AoA case, no vortex shedding is observed for all the tested reduced frequencies. For the 10° AoA case no vortex shedding occurs when $k<0.25$. Vortex shedding onset occurs when $k>0.25$. For the 10° AoA case, the peak-to-peak amplitude peaks at $k=0.4$ and then decreases as k increases. Figure 22 shows the lift history for $k=0.2$, 0.4, and 0.8. The largest variation appears at $k=0.4$. It can also be seen that the minimum lift value occurs at different points in the gust period for each of the k values, indicating a phase lag between the gust and lift.
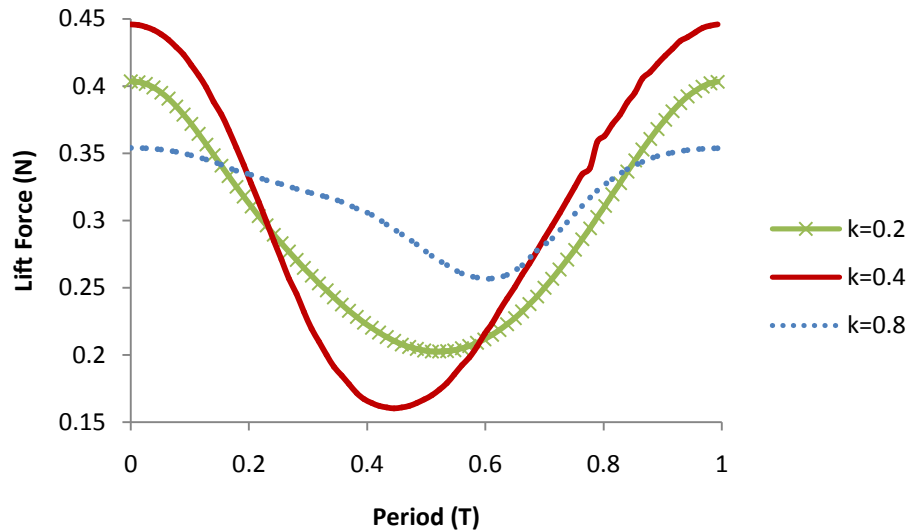
Figure 22 - Lift history over 1 period for a 10° AoA at $k = 0.2$, 0.4 and 0.8

Previous studies by Taira et al (2007), Colonius et al (2006), Joe et al (2010), and Brunton and Rowley (2010) noted that in 2-D computational studies there is a Hopf bifurcation that leads to exaggerated lift coefficients at higher angles of attack not seen in 3-D or experimental studies (see Figure 23). The onset of the Hopf bifurcation occurred in these papers when the flat plate began shedding vortices. The papers attribute the presence of the Hopf

bifurcation in the 2-D results but not the 3-D results to the interactions between the tip vortices

and the span wise flow causing the span wise flow to remain attached to the flat plate.
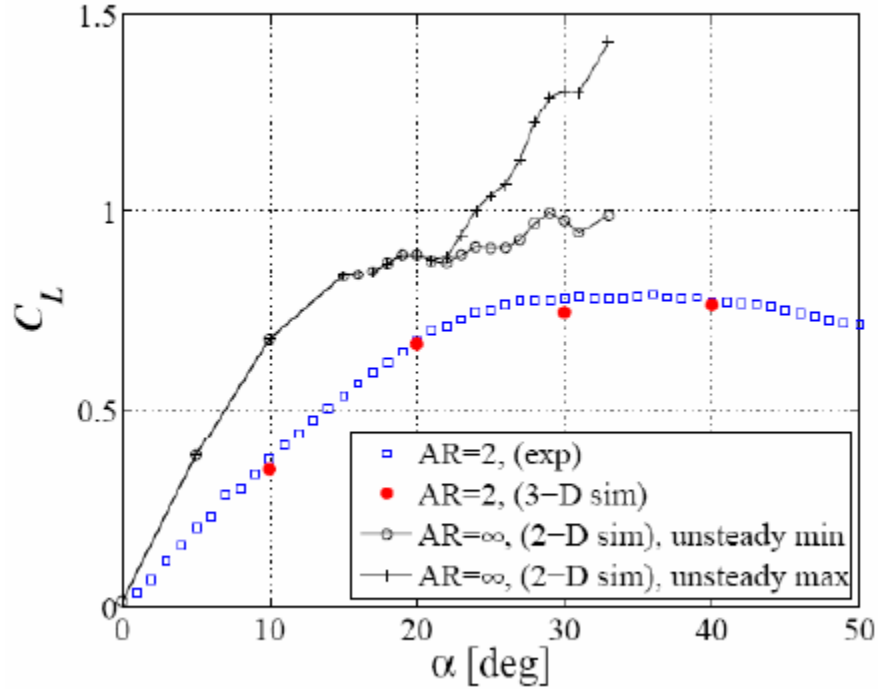
Figure 23 - Lift Coefficient versus AoA for 2-D Computational, 3-D Computational and Experimental Studies by Colonius et al. (2006)

As shown in Figure 19 and Figure 21, there was a jump in both the cycle averaged lift

and the peak-to-peak lift amplitude when the reduced frequency is larger than 0.2 for the case of

AoA of 10°. It was observed from the simulation that vortex starts to shed when k is larger than

0.2. It's hypothesized that the oscillating flow allows an early onset of the Hopf bifurcation

which artificially increases both the lift amplitude and the average lift. A 3-D study would be

needed to understand whether these results are accurate or an artifact of a 2-D simulation. It was

noted by Colonius et al. (2006) that for a 3-D simulation, the interaction between tip vortices and

the mid-span separated region prevented the vorticity shedding seen in the 2-D simulation. It

should be noted that the experimental results of (Williams et al. 2009b) showed a continued

increase in the peak-to-peak lift amplitude at the highest AoA (Figure 12) and that the observations of the Hopf bifurcation were conducted in steady flow.

Evidence of the onset of the bifurcation and vorticity shedding is presented in Figure 24 and Figure 25. Figure 24 shows a comparison of the vorticity contours for the k=0.2 and k=0.4 data from Figure 22 and Figure 25 shows the vorticity contours for k=0.2 and k=0.8.
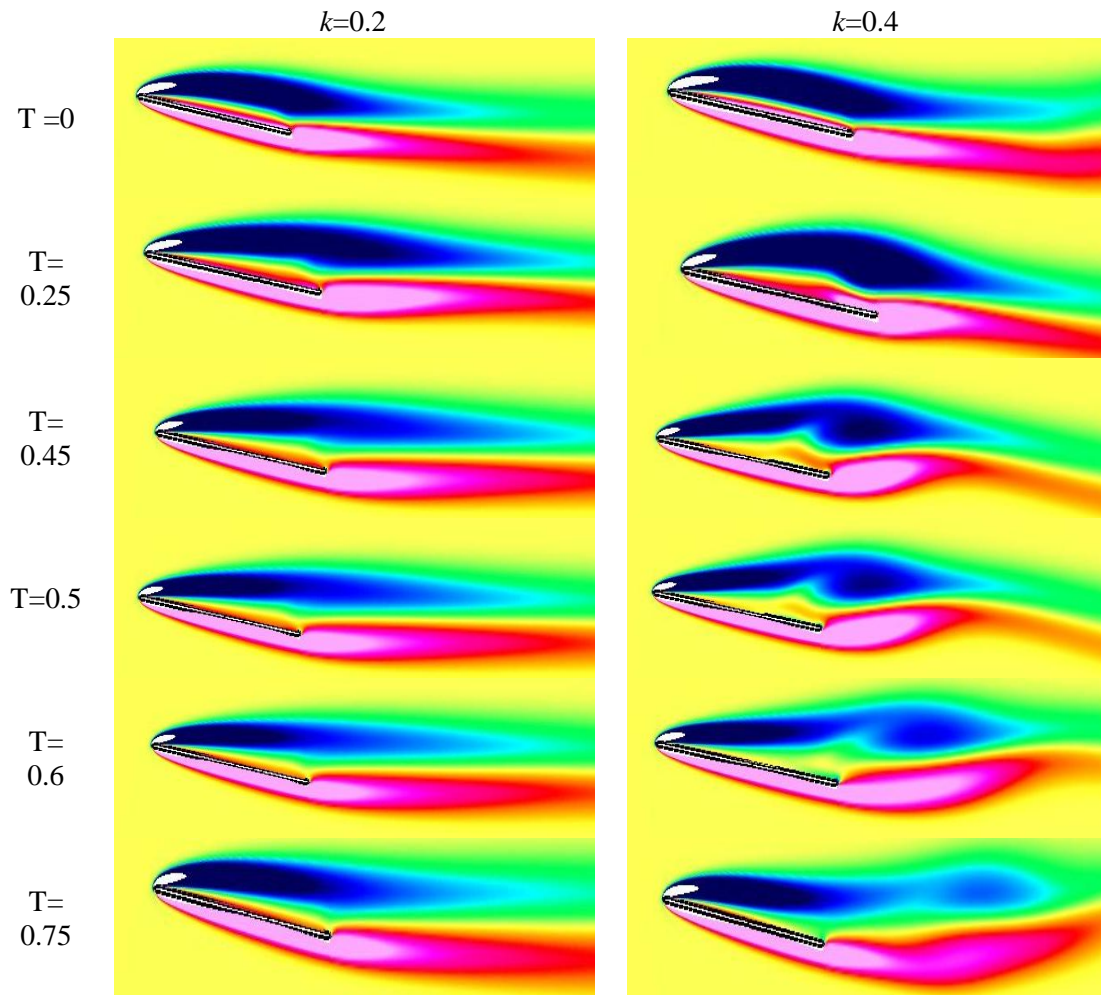
Figure 24 - Vorticity Contours of the k=0.2 and k=0.4 Data Sets from Figure 22.
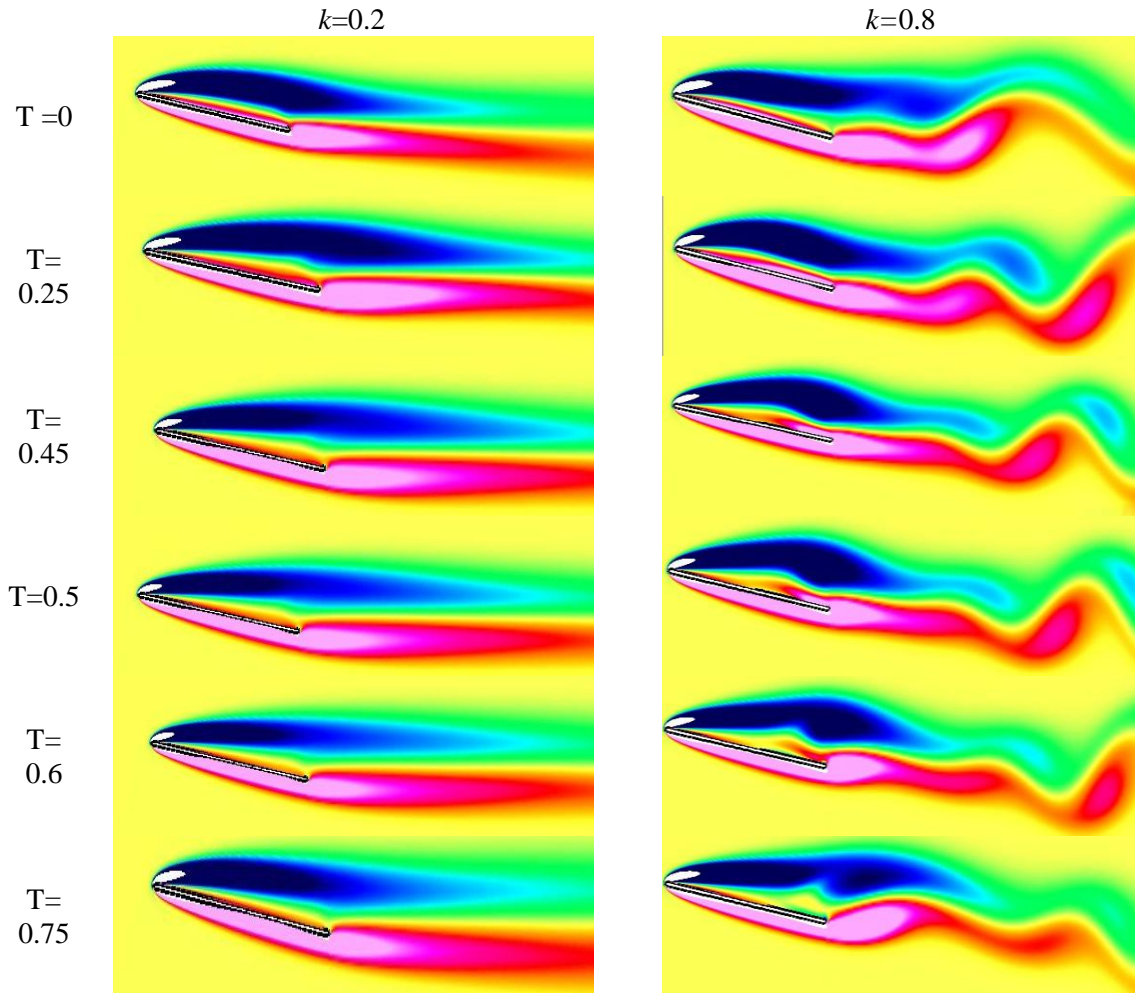
Figure 25 - Vorticity Contours of the k=0.2 and k=0.8 Data Sets from Figure 22.

From the figures it can be seen that at the reduced frequency of 0.2 there is no evidence

of vorticity shedding, whereas the simulations for reduced frequencies of 0.4 and 0.8 show clear

signs of vorticity shedding. An illustration of the impact that vorticity shedding has on the lift

force can be seen in Figure 26. For the data sets presented in Figure 22 vortices were being shed

at approximately the same frequency as the oscillations in the flow stream were occurring, in

Figure 26 the reduced frequency has been decreased to 0.02 while the amplitude of the

oscillations have been increased to 30% of the mean flow speed inducing shedding at this lower

reduced frequency. A simulation with an oscillation amplitude of 20% at the same reduced

frequency has been included for a comparison to a data set that doesn't exhibit vorticity

shedding.
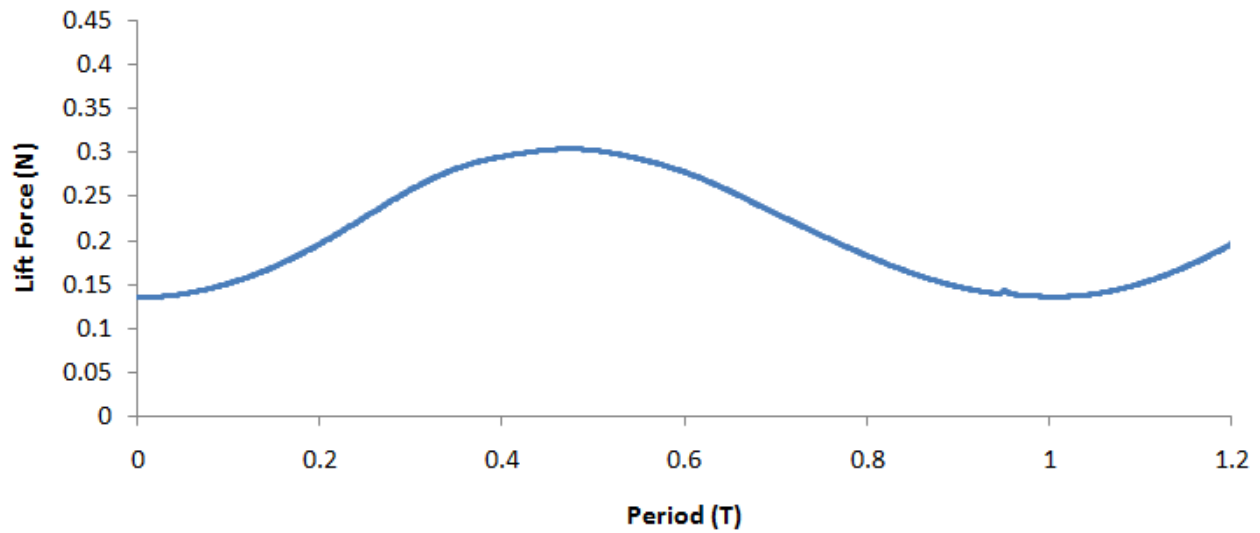
a) $a_u = 0.20$
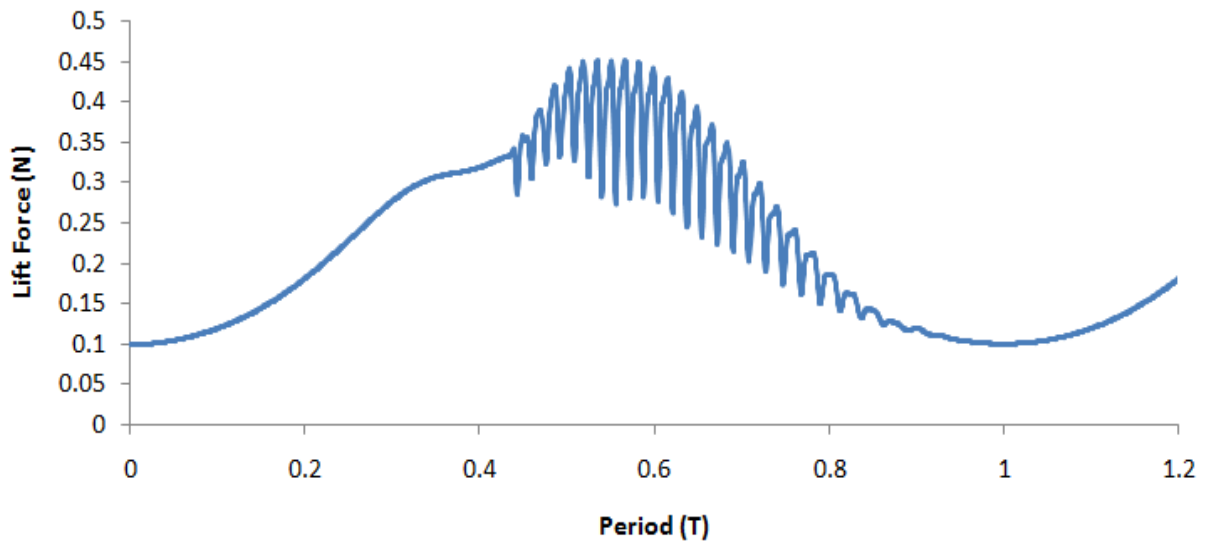
b) $a_u = 0.30$
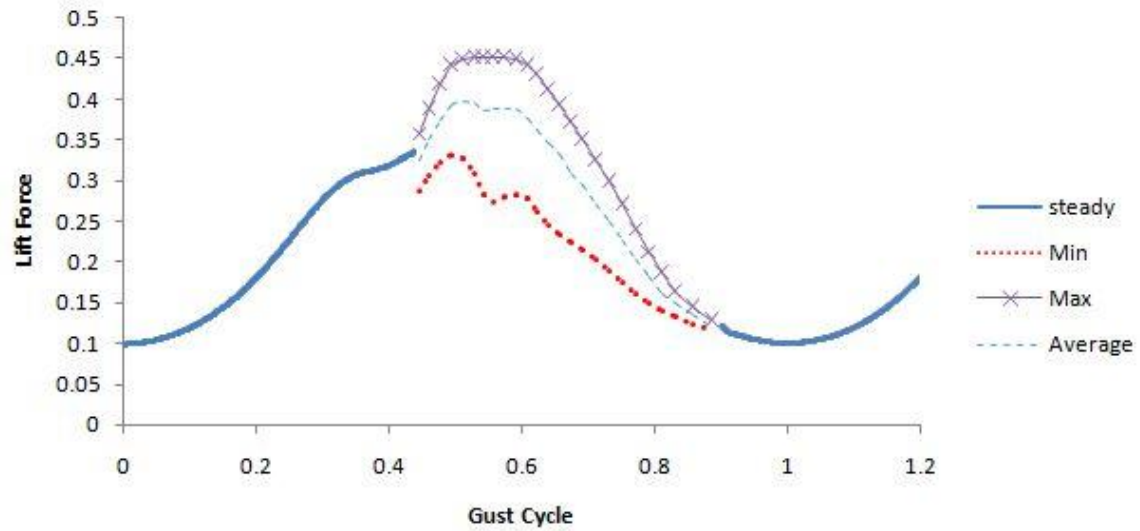
c) $a_u = 0.30$ with shed cycle averaged lift, max, and min.

Figure 26 - Force Histories of a Flat Plate at a Reduced Frequency of 0.02 with a) an Oscillation Amplitude of 0.20 b) an Oscillation Amplitude of 0.30 and c) the Shedding Cycle Averaged Lift, Max, and Min for b.

From Figure 26 it can be seen that once vorticity shedding has started to occur there is a jump in the average lift as well as a spike in the maximum lift.

54

E. Phase dependence based on the Reduced Frequency

Maintaining a smooth flight is often critical for MAV operations. If a real time control scheme were to be implemented to reduce variations caused by an oscillating freestream, then it would be important to understand the length of the delay between the changing freestream velocity and the resulting force variation. In this study the phase is defined as the time delay between the maximum freestream velocity and the maximum lift value. Figure 27 shows the lift history and freestream velocity history at AoA of 10° and a *k* value of 0.40 after the lift has reached a periodical nature. The maximum lift occurs at 0.125 of the period after the velocity maximum a 45° lag. Figure 28 shows the phase lag versus the reduced frequency for 6° and 10° angles of attack. Overall both cases show an increasing delay as the reduced frequency increases. It is noteworthy that the lift data for the 10° AoA starts to lead the gusting oscillation for *k* values that are less than 0.25.
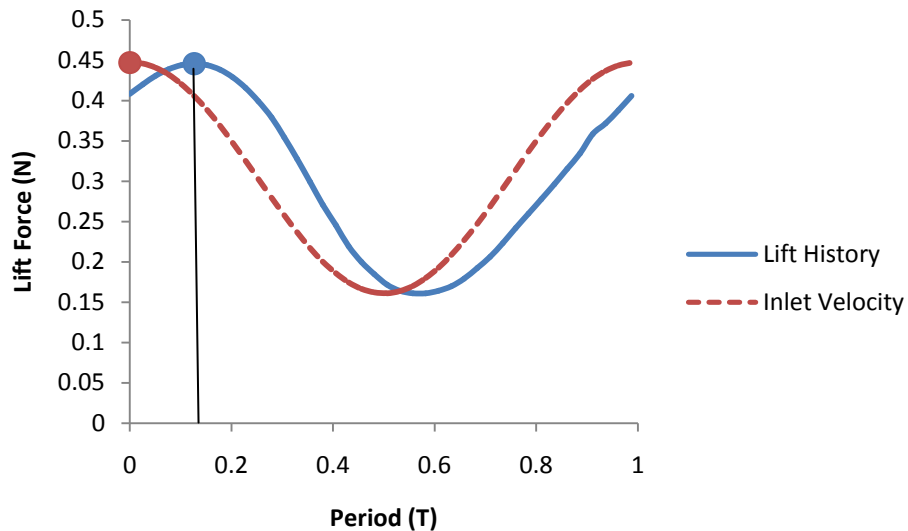
Figure 27 - Lift History and Inlet Velocity for 10° at *k*=0.4
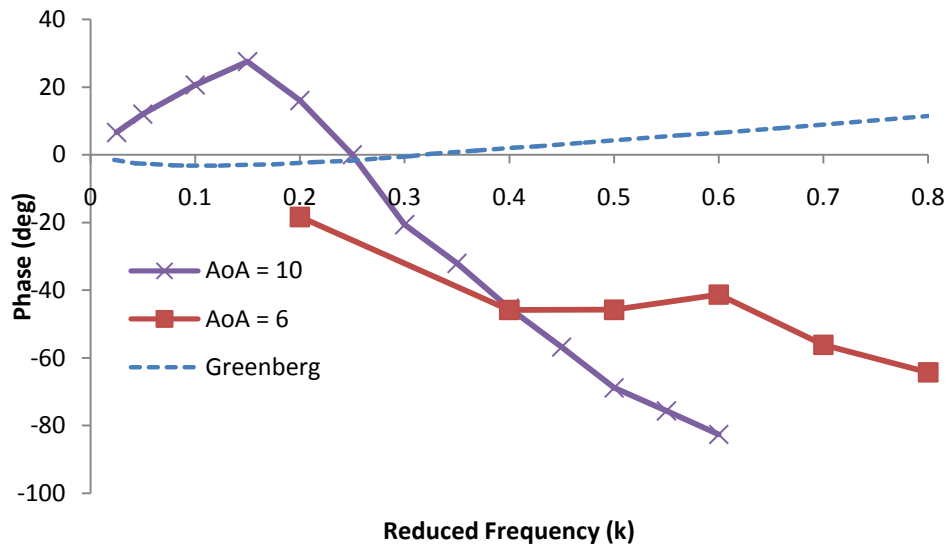
Figure 28 - Phase Lag vs. Reduced Frequency at 6° and 10° AoA.

The presence of a lag between the peak of the wind gust and peak lift means that if an active control scheme were to be employed there is a need for a delay based on when the peak freestream velocity occurs. Additionally, because the phase is dependent on the reduced frequency, the control would have to adapt to changes in the reduced frequency that would occur during operation by either increasing or decreasing the delay in order to adequately dampen out lift variations.

V.   CONCLUSIONS

A numerical analysis was performed to analyze the aerodynamic characteristics of a flat plate in gusting conditions. The numerical study was performed by solving the Navier-Stokes equations through numerical methods using the overture software package. The analysis showed the dependence of the time averaged lift on wind oscillation amplitude and oscillation frequency: high amplitude and high frequency lead to high time averaged lift. This characteristic is beneficial to MAV operation with MAVs potentially able to take advantage of the wind gusts to generate higher lift. Wind gust can also have detrimental effects on MAV flight: the high frequency gust causes high lift oscillation and leads to unstable flight. It was noted that an early onset of a Hopf bifurcation may be magnifying the aerodynamic response noted. To implement a control strategy to maintain a stable flight in gusting condition, it is critical to understand the correlation between phase delay and the reduced frequency. The analysis also showed that since the phase delay increases with reduced frequency, a successful control strategy would need to consider the variations in phase delay with the reduced frequency to maintain stable flight.

Transformation of w into z:

$$w = 2\mathrm{b}\cos(\theta) = \mathrm{b}(e^{i\theta} + e^{-i\theta}) = \mathrm{b}e^{i\theta} + \frac{\mathrm{b}^2}{\mathrm{b}e^{i\theta}}$$
$$\text{Therefore } z = \mathrm{b}e^{i\theta} = \mathrm{b}(\cos\theta + i\sin\theta)$$

Simplification of the potential from vertically symmetrical opposite signed sources:

$$\phi = \frac{m}{2\pi}\ln[(x - x_1)^2 + (y - y_1)^2] - \frac{m}{2\pi}\ln[(x - x_1)^2 + (y + y_1)^2]$$
$$= \frac{m}{2\pi}\ln\frac{(x - x_1)^2 + (y - y_1)^2}{(x - x_1)^2 + (y + y_1)^2}$$

Evaluation of the integration of 10 integrated over the transformed flatplate surface:

$$\phi_{top} = \frac{m}{2\pi}\int_{-\mathrm{b}}^{\mathrm{b}}\ln\frac{(x - x_1)^2 + (y - y_1)^2}{(x - x_1)^2 + (y + y_1)^2}dx_1$$
$$= -\frac{m}{2\pi}\cdot 2\sqrt{b^2 - x^2}\int_{-\mathrm{b}}^{\mathrm{b}}\frac{x_1 dx_1}{\sqrt{\mathrm{b} - x_1^2}(x - x_1)}$$
$$= m\sqrt{\mathrm{b}^2 - x^2}$$

Simplification of the pressure difference arising from the uniform flow over the transformed flat plate:

$$\triangle p = -\rho[\frac{1}{2}(u + \frac{\partial \phi_{top}}{\partial x})^2 + \frac{\partial \phi}{\partial t}] + \rho[\frac{1}{2}(u + \frac{\partial \phi_{top}}{\partial x})^2 - \frac{\partial \phi}{\partial t}]$$

$$\triangle p = -\rho[\frac{1}{2}[u^2 + 2u\frac{\partial \phi}{\partial x} + (\frac{\partial \phi}{\partial x})^2 - u^2 + 2u\frac{\partial \phi}{\partial x} - (\frac{\partial \phi}{\partial x})^2] + 2\frac{\partial \phi}{\partial t}]$$

$$\triangle p = -2\rho(u\frac{\partial \phi}{\partial x} + \frac{\partial \phi}{\partial t})$$

Solution for the integration of equation 22:

$$L = \int_{-b}^{b} \triangle p = \int_{-b}^{b} (\frac{-xu^2\alpha b}{\sqrt{b^2 - x^2} + -\dot{u}\alpha b}\sqrt{b^2 - x^2})dx$$

$$= \frac{-\pi}{2}\dot{u}\alpha b^2$$

Simplification of the potential due to the circulation of the two vortices:

$$\phi_\Gamma = \frac{\Gamma}{2\pi}[\arctan \frac{y}{x - X_0} - \arctan(\frac{y}{x - \frac{1}{X_0}})]$$

$$= \frac{\Gamma}{2\pi}[\arctan \frac{y(\frac{-1}{X_0} + X_0)}{x^2 - x(X_0 + \frac{1}{X_0}) + y^2 + 1}]$$

Evaluation of the derivative of the potential with respect to x:

$$\frac{\partial \phi_\Gamma}{\partial x} = \frac{\partial}{\partial x} \left[\frac{\Gamma}{2\pi} \arctan \frac{\sqrt{1-x^2}\sqrt{x_0^2-1}}{1-x \cdot x_0} \right]$$

$$= \frac{\Gamma}{2\pi} \sqrt{x_0^2-1} \frac{\frac{x}{(1-x\cdot x_0)\sqrt{1-x^2}} + \frac{x_0 \cdot \sqrt{1-x^2}}{(1-x\cdot x_0)^2}}{1 + \frac{(1-x^2)(x_0^2-1)}{(1-x\cdot x_0)^2}}$$

$$= \frac{\Gamma}{2\pi} \frac{\sqrt{x_0^2-1}}{(x_0-x)\sqrt{1-x^2}}$$

Evaluation of the derivative of the potential with respect to x_0:

$$\frac{\partial \phi_\Gamma}{\partial x_0} = \frac{\partial}{\partial x_0} \left[\frac{\Gamma}{2\pi} \arctan \frac{\sqrt{1-x^2}\sqrt{x_0^2-1}}{1-x \cdot x_0} \right]$$

$$= \frac{\Gamma}{2\pi} \sqrt{1-x^2} \frac{\frac{x_0}{(1-x\cdot x_0)\sqrt{x_0^2-1}} + \frac{x\sqrt{x_0^2-1}}{(1-x\cdot x_0)^2}}{1 + \frac{(1-x^2)(x_0^2-1)}{(1-x\cdot x_0)^2}}$$

$$= \frac{\Gamma}{2\pi} \frac{\sqrt{1-x^2}}{(x_0-x)\sqrt{x_0^2-1}}$$

Integration of equation 37 over the transformed flatplate:

$$L = \int_{-b}^{b} \triangle p = -2\rho u \frac{\Gamma}{2\pi} \int_{-b}^{b} \frac{x_0+x}{\sqrt{1-x^2}\sqrt{x_0^2-1}} dx$$

$$= -2\rho u b \frac{\Gamma}{2\pi} \frac{\pi x_0}{\sqrt{x_0^2-1}}$$

$$= -\rho u b \Gamma \frac{x_0}{\sqrt{x_0^2-1}}$$

Simplification of equation 42:

60

$$\frac{\Gamma}{2\pi}\frac{\sqrt{x_0^2-1}}{(x_0-x)\sqrt{1-x^2}} + \frac{-xu\alpha b}{\sqrt{1-x^2}} = 0$$

$$\frac{\Gamma}{2\pi}\frac{\sqrt{x_0^2-1}}{(x_0-x)\sqrt{1-x^2}} = \frac{xu\alpha b}{\sqrt{1-x^2}}$$

$$\frac{\Gamma}{2\pi}\frac{\sqrt{x_0^2-1}}{(x_0-x)} = xu\alpha b$$

Simplification of the equation C(k)

$$C(k) = \frac{\int_1^\infty \frac{x_0}{\sqrt{x_0^2-1}} U_0 e^{i\cdot k(\frac{\delta}{b}-x_0)} dx_0}{\int_1^\infty \sqrt{\frac{x_0+1}{(x_0-1)}} U_0 e^{i\cdot k(\frac{\delta}{b}-x_0)} dx_0}$$

$$= \frac{\int_1^\infty \frac{x_0}{\sqrt{x_0^2-1}} U_0 e^{i\cdot k(\frac{\delta}{b})} e^{(-i\cdot kx_0)} dx_0}{\int_1^\infty \sqrt{\frac{x_0+1}{(x_0-1)}} U_0 e^{i\cdot k(\frac{\delta}{b})} e^{(-i\cdot kx_0)} dx_0}$$

$$= \frac{\int_1^\infty \frac{x_0}{\sqrt{x_0^2-1}} e^{-i\cdot kx_0} dx_0}{\int_1^\infty \sqrt{\frac{x_0+1}{(x_0-1)}} e^{-i\cdot kx_0} dx_0}$$

Simplificiation of the ratio of lift in oscillatory flow to non-oscillatory flow

$$\frac{L}{L_0} = \frac{k}{2}a_u(Real(\cos\omega t - i\sin\omega t))$$
$$+ Real((F+i\cdot G)(1 - a_u(i\cos\omega t - \sin\omega t)) Real(1 - a_u(i\cos\omega t - \sin\omega t))$$

$$\frac{L}{L_0} = \frac{k}{2}a_u\cos\omega t + (1 + a_u\sin\omega t) Real(1 - a_u(F+iG)(i\cos\omega t - \sin\omega t)$$

$$\frac{L}{L_0} = \frac{k}{2}a_u\cos\omega t + (1 + a_u\sin\omega t)(1 + a_uF\sin\omega t + a_uG)\cos\omega t)$$

$$\frac{L}{L_0} = \frac{k}{2}a_u\cos\omega t + 1 + a_u\sin\omega t + a_uF\sin\omega t + a_u^2F\sin\omega t^2 + a_uG\cos\omega t + a_u^2G\cos\omega t\sin\omega t$$

$$\frac{L}{L_0} = (1 + \frac{a_u^2F}{2}) + a_u(\frac{k}{2} + G)\cos\omega t + a_u(1 + F)\sin\omega t - \frac{a_u^2F}{2}\cos 2\omega t + \frac{a_u^2G}{2}\sin 2\omega t$$

REFERENCES

Bowen, A. J., Flay, R.G.J., and Panofsky, H.A., "Vertical Coherence and Phase Delay Between Wind Components in Strong Winds Below 20 m," *Boundary-Layer Meteorology*, Vol. 26, 1983, pp. 313-324.

Brunton, S. and Rowley, C., "Unsteady Aerodynamic Models for Agile Flight at Low Reynolds Numbers," 48th AIAA Aerospace Sciences Meeting, AIAA Paper 2010-552, January 2010.

Colonius, T., Rowley, C., Tadmor, G., Williams, D., Taira, K., Dickerson, W., Gharib, M., and Dicinson, M., "Closed-Loop Control of Leading-Edge and Tip Vortices for Small UAV," September 2006.

Greenberg, J., "Airfoil in Sinusoidal Motion in a Pulsating Stream." NACA Technical Note 1326, 1947.

Guerrero, Joel., "Numerical Simulation of the Unsteady Aerodynamics of Flapping Flight,". Department of Civil, Environmental, Architectural Engineering, University of Genoa, 2009.

Henshaw, W. D., "A Fourth-Order Accurate Method for the Incompressible Navier-Stokes Equations on Overlapping Grids," *Journal of Computational Physics,* Vol. 113, number 1, 1994, pp. 13-25.

Henshaw, W., "The Overture Hyperbolic Grid Generator User Guide, Version 1.0," Technical Report, Lawrence Livermore National Laboratory, Research Report, 2003.

Henshaw, W., Kreiss, H., and Reyna, L., "A Fourth-Order Accurate Method for the Incompressible Navier-Stokes Equations," *Journal of Computers and Fluids,* Vol. 23, 1994, pp. 575-593.

Henshaw, W. and Peterson, N., "A Split-Step Scheme for the Incompressible Navier-Stokes Equations," Technical Report, Lawrence Livermore National Laboratory, Research Report, 2001.

Hord K. and Lian Y., "Numerical Investigation of the Aerodynamic and Structural Characteristics of a Corrugated Airfoil," AIAA Paper 2010-4624.

Joe, W., Colonius, T. and MacMynowski, D., "Feedback Control of Vortex Shedding From an Inclined Flat Plate," *Theoretical Computational Fluid Dynamics*, July 2010.

Langelaan, Bramesfeld, "Gust Energy Extraction for Mini- and Micro- Uninhabited Aerial Vehicles", *46th AIAA Aerospace Sciences Meeting,* AIAA Paper 2008-0223, Reno, Nevada 2008.

Lissaman, P. B. S. and Patel, C. K., "Neutral Energy Cycles for a Vehicle in Sinusoidal and Turbulent Vertical Gusts," 45th AIAA Aerospace Sciences Meeting and Exhibit, AIAA Paper 2007-863, American Institute of Aeronautics and Astronautics, Reno, Nevada, January 2007.

Lissaman, P., "Wind Energy Extraction by Birds and Flight Vehicles," 43rd AIAA Aerospace Sciences Meeting and Exhibit, AIAA Paper 2005-241, American Institute of Aeronautics and Astronautics, Reno, Nevada, January 2005.

McMasters, J. H., and Henderson, M. L., "Low Speed Single Element Airfoil Synthesis," *Technical Soaring,* Vol. 6, 1980, pp. 1- 21.

Munson, B., Young, D., and Okiishi, T., *Fundamentals of Fluid Mechanics*, 5th ed. John Wiley and Sons, 2006.

Patel, C. K. and Kroo, I., "Control Law Design for Improving UAV Performance using Wind Turbulence," AIAA Aerospace Sciences Meeting and Exhibit, AIAA Paper 2006-0231, American Institute of Aeronautics and Astronautics, Reno, Nevada, January 2006.

Spedding, G.R. and Lissaman, P.B.S., "Technical Aspects of Microscale Flight Systems," Journal of Avian Biology, Vol. 29, No. 4, 1998, pp. 458-468.

Taira, K., Dickson, W., Colonius, T., Kickinson, M. and Rowley, C., "Unsteadiness in Flow over a Flat Plate at Angle-of-Attack at Low Reynolds Numbers," 45th AIAA Aerospace Sciences Meeting and Exhibit, AIAA Paper 2007-710, January 2007.

Tannehill, J., Anderson, D. and Pletcher, R., *Computational Fluid Mechanics And Heat Transfer.* Taylor & Francis, 1997.

Theodorsen, Theodore, "Theory of Aerodynamic Instability and the Mechanism of Flutter," NACA Report Number 496, 1935.

Watkins, S., Milbank, J., Loxton, B. J., and Melbourne, W. H., "Atmospheric Winds and Their Implications for Micro Air Vehicles," AIAA Journal, Vol. 44, No. 11, November 2006, pp. 2591-2600.

Williams, Buntain, Quach and Kerstens, "Flow Field Structures behind a 3-D Wing in an Oscillating Freestream," 39th AIAA Fluid Dynamics Conference, AIAA Paper 2009-3690, 22 - 25 June 2009, San Antonio, Texas.

Williams, Quach, Buntain, Tadmor, Rowley, and Colonius, "Low-Reynolds Number Wing Response to an Oscillating Freestream with and without Feed Forward Control," 47th AIAA Aerospace Sciences Meeting Including The New Horizons Forum and Aerospace Exposition, AIAA paper 2009-143**,** 5 - 8 January 2009, Orlando, Florida.

Russell Prater
977 Eastern Parkway
Louisville, KY 40217
Cell: (502) 649-7996
rbprat01@louisville.edu

EDUCATION	**M. Eng. in Mechanical Engineering**	August 2011
	J.B. Speed School of Engineering, UofL, Louisville, KY	Graduate GPA 3.56/4.0
	Thesis – Numerical Simulation of a Flat Plate in Oscillating Flow	
	Dates attended 8/2005 – present	
	B.S. in Mechanical Engineering	August 2011
	J.B. Speed School of Engineering, UofL, Louisville, KY	Undergraduate GPA 3.525 / 4.0
	High School Diploma	
	Oldham County High School, Oldham, KY	May 2005
AWARDS	**University of Louisville Hallmark Award**	August 2005-August 2010
	Awarded to Kentucky student with GPA above 3.75/4.0 and minimum ACT of 30/36 or SAT of 1320/1600	
	University of Louisville Doctoral Fellowship	August 2011-Present
	Awarded to top departmental Ph.D. applicants	

EMPLOYMENT HISTORY

University of Louisville – Computational Fluid Dynamics Lab, Louisville, KY
Research Assistant   September 2009 - Present
- Performed analysis on flatplates at ultra-low Reynolds numbers in oscillating flow fields

Cummins Inc. – Product Engineering, Columbus, IN
Mechanical Co-op Engineer #2   August – December 2007
- Worked on investigation of engine failures in the product line.
- Created testing procedures for the investigation
- Performed tests to validate parts quality

Cummins Inc. – Value Engineering, Columbus, IN
Mechanical Co-op Engineer #1   January – May 2007
- Performed test on engine parts to ensure quality and conformity to engineering standards.

PUBLICATIONS

Russell Prater and Yongsheng Lian, "Numerical Investigation of the Aerodynamic Characteristics of a Flat Plate in Oscillating Flow, " AIAA-2010-0802, 40th Fluid Dynamics Conference and Exhibit, Chicago, Illinois, June 28-1, 2010

ACTIVITIES

Cardinal Computational Fluid Dynamics
Founder and Vice -President   April 2010-Present
- Registered Student Organization
- Arranged and organized student trips to conferences
- Managed laboratory personnel

University of Louisville Rugby Team
Founding Member   January 2008-Present
- Division III club in the Ohio Valley Rugby League for first 2 years
- Currently division II club team in the Ohio Valley Rugby League